DOKUZ EYLUL UNIVERSITY
GRADUATE SCHOOL OF NATURAL AND APPLIED SCIENCES

INVESTIGATION OF HIGH AND LOW TEMPERATURE CORROSION BEHAVIOUR OF NICKEL-BASE ALLOYS

by
Esra DOKUMACI

July, 2006

İZMİR

INVESTIGATION OF HIGH AND LOW TEMPERATURE CORROSION BEHAVIOUR OF NICKEL-BASE ALLOYS

A Thesis Submitted to the
Graduate School of Natural and Applied Sciences of Dokuz Eylül University
In Partial Fulfillment of the Requirements for the Degree of Master of Science
in Metallurgy and Materials Engineering, Metallurgy and Materials Program

by
Esra DOKUMACI

July, 2006
İZMİR

M.Sc THESIS EXAMINATION RESULT FORM

We have read the thesis entitled **"INVESTIGATION OF HIGH AND LOW TEMPERATURE CORROSION BEHAVIOUR OF NICKEL-BASE ALLOYS"** completed by **ESRA DOKUMACI** under supervision of **ASSOC. PROF. A. BULENT ONAY** and we certify that in our opinion it is fully adequate, in scope and in quality, as a thesis for the degree of Master of Science.

Assoc. Prof. A.Bülent ÖNAY

Supervisor

Prof. Dr. Ahmet ÇAKIR

(Jury Member)

Yrd. Doç. Dr. Ufuk MALAYOĞLU

(Jury Member)

Prof. Dr. Cahit HELVACI

Director

Graduate School of Natural and Applied Sciences

ACKNOWLEDGMENTS

I cordially would like to express my thanks to my supervisor, Assoc. Prof. A. Bülent ÖNAY for his support, interest and encouragement.

I also would like to thank my colleagues and my family for their cooperation, assistance and patience.

Esra DOKUMACI

INVESTIGATION OF HIGH AND LOW TEMPERATURE CORROSION BEHAVIOUR OF NICKEL-BASE ALLOYS

ABSTRACT

In this study, both low (T<1000^{o}C) and high temperature (T>1000^{o}C) oxidation behavior of two commercial Ni alloys containing more than 10% Mo, a refractory metal, is investigated. For this purpose, Hastelloy C-22 ve C-276 alloy samples were exposed to the stagnant air environment of a high temperature furnace for predetermined times. Extent of alloy oxidation was determined from sample mass change measurements while morphologies and chemical compositions of the product oxide scales were investigated with a scanning electron microscope (SEM) equipped with a backscattered electron (BE) detector and an energy dispersive spectroscopy (EDS) detector. A x-ray diffractometer (XRD) was also used to identify the crystalline phases in the scales developed over the alloy samples. Important findings of this study can be summarized as follows: Significant mass changes due to oxidation was observed only at temperatures above 1000^{o}C. Although oxide scales with similar microstructures and chemical compositions formed over both alloy samples, the C-276 alloy sample with the higher Mo content had larger amount of scale spallation (detachment). Furthermore, Mo-rich areas were found at scale locations where spallation took place. Detection of Mo over the inner surfaces of the ceramic crucible containing the C-276 sample indicated that Mo was preferentially removed, by evaporation, from the alloy sample during the high temperature tests. This observation suggested that Mo in the alloy affected scale spallation. The present study also indicated that Ni-Mo and Ni-W intermetallic phases in the as-received Ni-base alloys might have also affected their oxidation behavior. These results clearly showed that presence of a large amount of refractory elements in an alloy can decrease its oxidation resistance at high temperatures.

Key words: high temperature corrosion, molybdenum, nickel alloy, SEM

NİKEL ESASLI ALAŞIMLARIN YÜKSEK VE DÜŞÜK SICAKLIK KOROZYON DAVRANIŞLARININ İNCELENMESİ

ÖZ

Bu çalışmada, %10'dan (ağırlık olarak) fazla refrakter metal Molibden (Mo) içeren iki ticari Ni alaşımının düşük ($T<1000^oC$) ve yüksek ($T>1000^oC$) sıcaklık oksidasyon davranışları incelenmiştir. Bu amaçla, Hastelloy C-22 ve C-276 alaşımlarından hazırlanan numuneler, durgun hava ortamındaki bir fırın içerisinde belli sıcaklıklarda önceden belirlenen sürelerde tutulmuştur. Alaşımların oksitlenme özellikleri, nicel olarak, numunelerin deney sonrasındaki ağırlık değişimleriyle ölçülmüştür. Bunun yanı sıra, geri saçılmış elektron (BE) detektörü ve enerji dağılım spektroskopuna (EDS) sahip bir taramalı elektron mikroskobu (SEM) ile X-ışınları difraktometresi (XRD) kullanılarak, deneyler sonrasında numune yüzeylerinde oluşan oksit tabakalarının morfolojileri, kimyasal kompozisyonları ve kristal yapıları incelenmiştir. Çalışmanın önemli sonuçları şunlardır: Alaşımlarda kayda değer miktarlarda bir oksitlenme 1000^oC'nin üzerindeki sıcaklıklarda olmuştur. Yüzeyde oluşan oksit tabakalarının mikroyapı ve kimyasal kompozisyonları benzer olmasına karşın, Mo içeriği daha fazla olan C-276 numunesinin yüzeyinden dökülen oksit tabakaları daha fazladır. Dökülmelerin olduğu oksit bölgelerinin Molibdence daha zengin olduğu gözlemlenmiştir. Yüksek sıcaklık deneyleri sonrasında, Mo elementinin, numuneleri barındıran seramik kapların iç yüzeylerinde de saptanması, Mo'nin yüksek sıcaklıklarda buharlaşma yoluyla numuneden ayrıldığını göstermiştir. Dolayısıyla, yüzey tabakalarının dökülmesinde alaşımın Mo miktarının etkisi olduğu anlaşılmış, bu nedenle yüksek miktarda Mo gibi refrakter metal içeren alaşımların yüksek sıcaklık oksitlenme dirençlerinin düşük olacağı görülmüştür. Ayrıca, ticari olarak üretilen bu tip alaşımların mikroyapılarında bulunan Ni-Mo ve Ni-W içerikli intermetalik fazların da alaşımların yüksek sıcaklık oksitlenme dirençlerini olumsuz olarak etkileyebilecekleri bu çalışmada anlaşılmıştır.

Anahtar sözcükler: yüksek sıcaklık oksidasyonu, molibden, nikel alaşımları, SEM

CONTENTS

Page

CHAPTER ONE
INTRODUCTION

Ni-base alloys are currently used as high temperature materials in many important engineering systems like aircraft engines, industrial furnaces and electric power generating gas turbines. However, in most cases, these alloys are being used at temperatures over which creep of the material will be an important concern. To overcome this deficiency, alloy systems based on refractory elements like Mo and Nb as well as Cr and Ir are being investigated extensively as the next generation high temperature metallic materials (Akhtar, Hegde & Reed, 2006; Kawagishi & et. al., 2006; Hebsur & et. al., 1989). However, one major drawback for the application of the refractory alloys based on Mo and Nb is their poor resistance to oxidation (scaling) in oxygen-containing environments like air. Thus, methods to improve oxidation-resistance of these alloys are urgently needed. (Habazaki & et. al., 1999)

To understand and improve the high temperature environmental resistance of Mo and Nb-base alloys, a research project on these alloys has been initiated by a group in the Metallurgical and Materials Engineering department of the Dokuz Eylul University. In this project, production and environmental testing of Mo and Nb-base alloys are planned.

In this current study, both low ($T<1000^oC$) and high temperature ($T>1000^oC$) oxidation behavior of two commercial Ni-base alloys (C-22 and C-276) was investigated. These alloys were chosen because they contain more than %10 Mo (by weight) in their microstructure. By investigating these alloys, it is aimed to understand the effect of Mo in alloy oxidation and scale formation at high temperatures. Results of this study are therefore hoped to be useful in developing Mo-base alloys with improved oxidation resistance in the research project mentioned above.

In this work, two Mo-containing alloys C-22 and C-276 were exposed to a stagnant air environment both at low (500^oC, 700^oC, 800^oC, 900^oC) and high

(1150^{o}C) temperatures. At low temperatures, the oxidation times were shorter (about 30 min.). In these short term tests, the objective was to follow the development of the oxide scale as a function of temperature and observe the effect of Mo on the scale development. On the other hand, high temperature tests were conducted for both short and long times. The long-term test also involved thermal cycling of the alloy samples. These tests yielded results related to the location of Mo in the oxidation products, effect of Mo on scale spallation (scale detachment from the surface) as well as the evaporation of Mo-rich corrosion products from the alloy samples.

Observations made during this study such as the volatilization of Mo during oxidation complicates the high temperature oxidation resistance of Mo-containing alloys as discussed also by other researchers in the literature.

In this study, discontinuous measurement of sample weight changes was used as a method to observe the extent of oxidation and scale spallation. Also, a SEM equipped with a back scattered electron (BE) detector and an EDS detector was used extensively to investigate morphologies and chemical compositions of the oxidation products grown over the samples. XRD was also used to study the crystal structures of the selected oxide scales.

Major findings of this work can be summarized as follows:

1. Significant oxide scale formation on both alloy samples were observed only at temperatures above 1000^{o}C.

2. Over both alloys, multi-component, multi-structure scales containing Ni and Cr-rich oxides developed. Mo was present in scales, but its distribution was not uniform.

3. Oxide scale spallation was more severe for the C-276 alloy which has a lower Cr but a higher Mo content. SEM investigations suggested that scale spallation took place at Mo-rich areas in the scale.

4. Mo was removed from the alloys, especially from the Mo-rich C-276 alloy during oxidation at high temperature. Formation and volatization of gaseous Mo-oxides (possibly as MoO_3) is thought to be an important cause for the observed weight changes and scale spallation.

5. Alloys used in this study contained intermetallic compounds (in the form of Ni_xMo_y and Ni_xW_y) in as-received condition. In the Mo-rich C-276 alloy, larger particles of such second-phase precipitates were present. Although not definitive, such precipitates are believed to have affected scale spallation observed for these Mo-containing alloys.

6. In any oxidation-resistant Mo-rich alloy development work, all these observed effects of Mo on alloy oxidiation should be taken into account.

CHAPTER TWO
HIGH TEMPERATURE ALLOYS

2.1 Superalloys

2.1.1 General Information

A superalloy is an alloy developed for elevated temperature service, usually based on group VIIIA elements, where relatively severe mechanical stressing is encountered and where high surface stability is frequently required at high temperatures in corrosive environments (Betteridge & Shaw, 1987).

Superalloys are heat-resisting alloys based on nickel, nickel-iron, or cobalt that exhibit a combination of mechanical strength and resistance to surface degradation. Superalloys are primarily used in gas turbines, coal conversion plants, and chemical process industries, and for other specialized applications requiring heat and/or corrosion resistance. The modern high-performance aircraft (jet) engine could not operate without the major advances made in superalloys development over the past 50 years. A noteworthy feature of nickel-base alloys is their use in load-bearing applications at temperatures in excess of 80% of their incipient melting temperatures, a fraction that is higher than for any other class of engineering alloys (Stoloff, 1990).

2.1.2 Applications of Superalloys

Applications of superalloys are categorized below; the bulk of tonnage is used in gas turbines:

- aircraft gas turbines: disks, combustion chambers, bolts, casing, shafts, exhaust systems, cases, blades, vanes, burner cans, afterburners, thrust reversers
- steam turbine power plants: bolts, blades, stack gas reheathers
- reciprocating engines: turbochargers, exhaust valves, hot plugs, valve seat inserts

- metal processing: hot-work tools and dies, casting dies
- medical applications: dentistry uses, prosthetic devices
- space vehicles: aerodynamically heated skins, rocket engine parts
- heat-treating equipment: trays, fixtures, conveyor belts, baskets, fans, furnace mufflers
- nuclear power systems: control rod drive mechanisms, valve stems, springs, ducting
- chemical and petrochemical industries: bolts, fans, valves, reaction vessels, piping, pumps
- pollution control equipment: scrubbers
- metals processing mills: ovens, after-burners, exhaust fans
- coal gasification and liquefaction systems: heat exchangers, reheaters, piping (Stoloff, 1990).

2.2 Nickel-base Alloys

2.2.1 Evolution of Nickel-base Alloys

Like iron and copper, nickel has been used in alloys since the dawn of civilization. However, in contrast to steels, brasses and bronzes, nickel alloys are recent newcomers to the chemical industry.

Over the past three decades superalloys have played significant roles in advanced technological applications particularly in the aircraft and power generation fields. Solid solution-strengthened nickel- and cobalt- base alloy with unique combinations of mechanical strength, environmental resistance and fabricability have been of particular importance in the manufacturing of combustor components of gas turbine engines. Nickel-base superalloys are the most complex, the most widely used for the hottest parts, and, to many metallurgists, the most interesting of all superalloys. They currently constitute over 50% of the weight of advanced aircraft engines (Tawancy & et. al., 1984).

The first nickel alloy of significant commercial importance was Alloy 400, developed and marketed by the International Nickel Co. (now Inco Alloys International) in 1905 under the MONEL trademark. The next important milestone was the emergence around 1930 of Ni-Mo Alloy B and Ni-Cr-Mo-W Alloy C. Their developer, the Haynes Stellite Co. (now Haynes International Inc.), trademarked both of these materials as HASTELLOY. The next important rung in the evolutionary ladder of nickel-base alloys came from Inco, with the advent of Ni-Cr-Fe Alloy 600 in 1931 and Ni-Fe-Cr in 1949, respectively named INCONEL and INCOLOY (Tawancy & et. al., 1984).

Capitalizing on the familiarity and reputation of these original trademarks, Inco and Haynes are now marketing a combined total of about 50 corrosion- and heat-resistant alloys in the MONEL, INCONEL, INCOLOY and HASTELLOY families.

2.2.2 Properties and Types of Nickel-base Alloys

Nickel and nickel-base alloys are vitally important to modern industry because of their ability to withstand a wide variety of severe operting conditions involving corrosive enviroments, high temperatures, high stresses, and combinations of these factors. Pure nickel is ductile and tough because it posseses a face-centered cubic (fcc) crystal structure up to its melting point. Therefore, nickel and its alloys are readily fabricated by conventional methods, and they offer freedom from the ductile-to brittle transition behavior of most body-centered cubic (bcc) and noncubic metals. Nickel has good resistance corrosion in the normal atmosphere, in natural freshwaters and in deaerated nonoxidaizing acids, and it has excellent resistance to corrosion by caustic alkalies.

The compositions of many representative nickel-base wrought alloys are listed in Table 2.1. They can be categorized as nickel-iron-base alloys, in which nickel is the major solute element, or nickel-base, in which at least 50% Ni is present (Sridhar, 1987).

Table 2.1 Nominal composition of nickel-base alloys (Sridhar, 1987)

Common alloy designation	UNS designation	Chemical composition										
		C	Nb	Cr	Cu	Fe	Mo	Ni	Si	Ti	W	Other
Nickel												
200…….	N02201	0.1	….	….	0.25max	0.4max	….	99.2min	0.15	0.1max	….	….
201…….	N02301	0.002	….	….	0.25max	0.4max	….	99.2min	0.15	0.1max	….	….
Nickel – Copper												
400…….	N04400	0.15	….	….	31.5	1.25	….	bal	0.5	….	….	….
R 405…….	N04405	0.15	….	….	31.5	1.25	….	bal	0.5	….	….	0.0435
Nickel –molybdenum												
B-2…….	N10665	0.01	….	1.0max	….	2.0max	28	bal	0.1	….	….	….
B……..	N10001	0.05	….	1.0max	….	5.0	28	bal	1.0	….	….	….
Nickel-chromium –iron												
600…….	N06600	0.08	….	16.0	0.5max	8.0	….	bal	0.5	0.3max	….	….
601…….	N06601	….	….	23.0	….	14.1	….	bal	….	….	….	1.35Al
800…….	N08800	0.1	….	21.0	0.75max	44.0	….	32.5	1.0	0.38	….	….
800H……..	N08810	0.08	….	21.0	0.75max	44.0	….	32.5	1.0	0.38	….	….
Nickel-chromium-iron-molybdenum												
825…….	N08825	0.05	….	21.5	2.0	29.0	3.0	42	0.5	1.0	….	
G……	N06007	0.05	2.0	22.0	2.0	19.5	6.5	43	1.0	….	1.0max	….
G-2/2550	N06975	0.03	….	24.5	1.0	20.0	6.0	48	1.0	1.0	….	….
G-3…….	N06985	0.015	0.8	22.0	2.0	19.5	7.0	44	1.0	….	1.5max	….
H……	……	0.03	….	22.0	….	19.0	9.0	42	1.0	….	2.0	….
G-30……..	N06030	0.03	0.8	29.5	2.0	15.0	5.5	43	1.0	….	2.5	….
Nickel-chromium-molybdenum-tungsten												
N……	N10003	0.06	….	7.0	0.35max	5.0max	16.5	71	1.0	0.5max	0.5max	….
W……	N10004	0.12	….	5.0	….	6.0	24.0	63	1.0	….	….	….
625…….	N06625	0.1	4.0	21.5	….	5.0max	9.0	62	0.5	….	….	….
690…….	N06690	0.02	….	29.0	….	10.0	….	61	….	0.3	….	….
C-276……	**N10276**	**0.01**	**….**	**15.5**	**….**	**5.5**	**16.0**	**57**	**0.08**	**….**	**0.40**	**….**
C-4…….	N06455	0.01	….	16.0	….	3.0max	15.5	65	0.08	….	….	….
C-22…….	**N06022**	**0.015**	**….**	**22.0**	**….**	**3.0max**	**13.0**	**56**	**0.08**	**….**	**0.30**	**….**
ALLCORR	N06110	0.15	2.0max	30.0	….	….	10.0	53	….	1.5max	4.0max	….
Nickel-silicon												
D……	……	0.12	….	1.0max	3.0	2.0max	….	86	9.5	….	….	….
Precipitation hardening												
K-500…….	N05500	0.25	….	….	29.0	2.0max	….	63	0.5max	0.6	….	2.7Al
R-41……..	N07041	0.09	….	19.0	….	5.0max	10.0	52	0.5max	3.1	….	1.5Al
718……	07718	0.05	5.0	18.0	….	19	3.0	53	….	0.4max	….	….
X-750……	N07750	…..	0.9	15.5	….	7.0	….	bal	….	2.5	….	….
925……	N09925	0.02	….	21.0	2.0	28	3.0	43	….	2.1	….	….

Refractory elements tungsten and molybdenum are added to increase high temperature stiffness. These additions play dual roles as strengtening solutes and carbides formers. The function of the various elements in nickel alloys are

summarized in Table 2.2 Effect of alloying elements on nickel-base alloys are given in Table 2.3.

Table 2.2 Role of elements in nickel-base alloys (Mankins & Lamb, 1990)

Effect	Addition Elements
Solid- solution strengtheners	Co, Cr, Fe, Mo, W, Ta
Carbide form	
MC type	W, Ta, Ti, Mo, Nb
M_2C_3 type	Cr
$M_{23}C_6$ type	Cr, Mo, W
M_6C type	Mo, W
Carbonitrides	
M(CN) type	C, N
Forms γ' Ni_3(Al, Ti)	Al, Ti
Raises solvus temperature of γ'	Co
Hardening precipitation and intermetallics	Al, Ti, Nb
Forms γ" (Ni_3Nb)	Nb
Oxidation resistance	Al, Cr
Improves hot corrosion resistance	La, Th
Sulfidation resistance	Cr
Increases rupture ductility	B, Zr
Causes grain-boundary segregation	B, C, Zr

Table 2.3 Alloying elements and their effects in nickel-base alloys

Element	Effects on alloy
Chromium	*Improves oxidation resistance provided temperature does not exceed 950°C for long periods, *Decreases carbon ingress-helps carburization resistance, *Detrimental to fluorine-containing environment at high temperature, *Detrimental to nitriding resistance; increases high temperature strength, *High chromium beneficial to oil ash corrosion and attack by molten glass, *Improves sulfidation resistance.
Silicon	*Improves resistance to oxidation, nitriding, sulfidation, and carburizing, *Synergically acts with chromium to improve scale resilience,

	*Detrimental to non-oxidizing chlorination resistance.
Aluminum	*Independently and synergically with chromium raises oxidation resistance,
	*Helps sulfidizing resistance; detrimental to nitriding resistance.
Titanium	*Detrimental to nitriding resistance.
Niobium	*Increases short-term creep strength; may be beneficial in carburizing,
	*Detrimental to nitriding resistance.
Molybdenum/ Tungsten	*Improves high temperature strength, good in reducing chlorination resistance,
	*Improves creep strength,
	*Detrimental for oxidation resistance at higher temperature.
Nickel	*Improves carburization, nitriding and chlorination resistance,
	*Detrimental to sulfidation resistance.
Carbon	*Improves strength; helps nitridation resistance,
	**Beneficial to carburization resistance,
	*Oxidation resistance adversly affected.
Yttrium/ Rare earths	*Improves adherence and spalling resistance of oxide layer, hence improves oxidation, sulfidation, carburization resistance.
Manganese	*Slight positive effect on high temperature strength and creep,
	*Detrimental to oxidation resistance; increases solubility of nitrogen.
Cobalt	*Reduces rate of sulfur diffusion, hence helps with sulfidation resistance,
	*Improves solid solution strength.

2.2.3 Hastelloy C–276 Alloy

Hastelloy C-276 is a nickel-molybdenum-chromium alloy with an addition of tungsten having excellent corrosion resistance in a wide range of severe environments. Physical and mechanical properties are given in Table 2.4. The high molybdenum content makes the alloy especially resistant to pitting and crevice corrosion. C-276 alloy has excellent resistance to localized corrosion and to both oxidizing and reducing media. Because of its versatility, C-276 alloy can be used where upset conditions are likely to occur or in multipurpose plants. Hastelloy C-276 alloy has excellent resistance to a wide variety of chemical process environments,

including strong oxidizers such as ferric and cupric chlorides, hot contaminant media chlorine, formic and acedic acids, acetic anhydrite, seawater and brine solution. It is used in flue gas desulfirization systems because of its excellent resistance to sulfur compounds and chloride ions encountered in most scrubbers. C-276 alloys has excellent resistance to pitting and to stress corrosion cracking. It is also one of the few materials that withstands the corrosive effects of wet chlorine gas, chlorine dioxides. The low carbon content minimizes carbide precipitation during welding to maintain corrosion resistance in as-welded structures. Fig. 2.1 shows the effects of Mo and Ni content on the corrosion resistance of varies alloys (Mankins & Lamb, 1990).

Table 2.4 Properties of Hastelloy C-276 and C-22 (from Alloy Wire International Page)

Properties		Hastelloy C-276	Hastelloy C-22
Density (g/cm^3)		8.89	8.69
Coefficient of Expansion ($\mu m/m^oC$)		11.2	12.6
Melting Point (^oC)		1370	1399
Rigidity Modulus (kN/mm^2)		78.6	78.6
Young Modulus (kN/mm^2)		205.5	205.5
Approx. Tensile (N/mm^2)	Annealed	850–1050	900–1100
	Spring Temper	1300–1600	1400–1700

Applications of C-276;

- Components exposed to sour gas,
- Equipment for flue-gas desulfurisation plants,
- Evaporators, heat exchangers, filters and mixers used in sulfuric acid environments,
- Sulfuric acid reactors,
- Organic chloride process equipment,
- Equipment for processes utilizing halide or acid catalysts,
- Digesters and bleach plants in the paper industry.

2.2.4 Hastelloy C-22 Alloy

Hastelloy C-22 alloy is a nickel-chromium-molybdenum with outstanding resistance to pitting, crecive corrosion and stress-corrosion cracking. In Table 2.4 properties of Hastelloy C-22 are given. C-22 alloy has outstanding resistance to pitting, crevice corrosion, and stress corrosion cracking. It has excellent resistance to oxidizing aqueous media including wet chlorine and mixtures containing nitric acid or oxidizing acids with chloride ions. Also, C–22 alloy offers optimum resistance to environments where reducing and oxidizing conditions are encountered in process streams. Because of such versatility it can be used where upset conditions are likely to occur or in multi-purpose plants. (Mankins & Lamb, 1990)

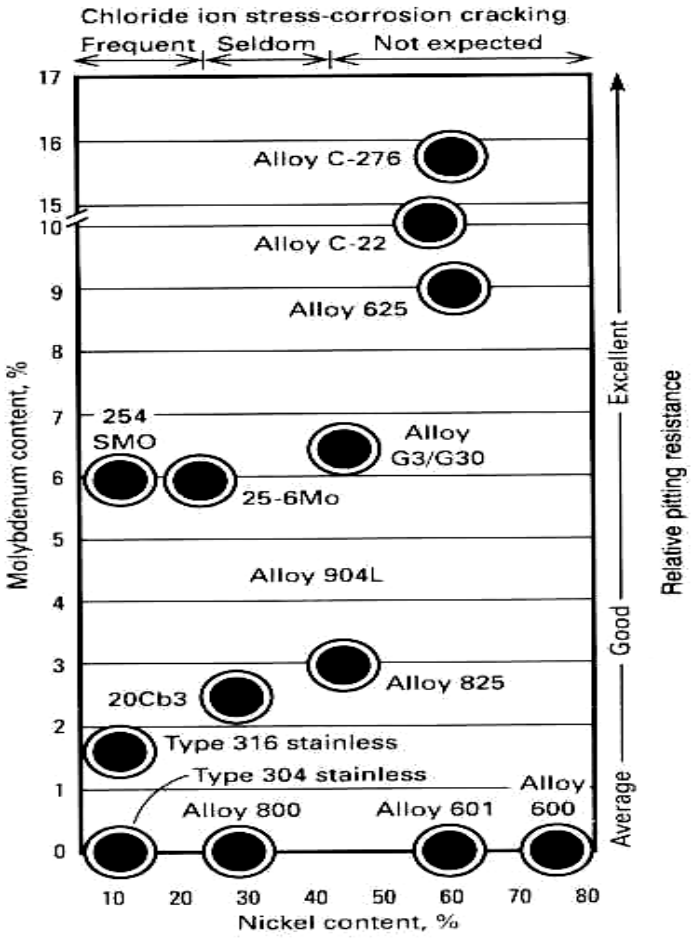

Figure 2.1 Effect of Mo and Ni contents on the corrosion resistance of selected commercial alloys (Mankins &Lamb,1990)

Applications of C–22;

- Chlorine spargers, chlorination systems,
- Circuit board etching equipment,
- Complex acid/chemical mixtures (phosphoric, sulfuric and acetic acid),
- Fans and blowers,
- Galvanizing line equipment,
- Geothermall wells,
- HF furnaces,
- Nuclear fuel reprocessing,
- Heat exchangers.

2.3 Refractory Metals

High melting temperatures of the refractory metals give them the capability of performing useful engineering functions at temperatures far beyond those possible with conventional alloys. This important characteristic makes this class of materials technologically important. The metallic elements generally referred to as the major refractory metals are niobium (Nb) and tantalum (Ta) of group VA, and molybdenum (Mo) and tungsten (W) of group VIA of the Periodic Table. Table 2.5 compares the physical, thermal, electrical, magnetic and optical properties of pure refractory metals. Fig. 2.2, 2.3 and 2.4 compare the temperature dependent ultimate tensile strengths, elastic moduli and creep-rupture strengths of the refractory metals (Buckman, 1988 ; Davis, 1997).

The pure refractory metals generally do not exhibit sufficient strenght at elevated temperatures for most engineering applications. Comparative high temperature data for refractory metals are given in Table 2.6 (Davis, 1997). But through alloying it is possible to improve the high temperature strength of the refractory metals. Alloy strengthening has been a topic of extensive study. Alloying effects related to improvement of elevated-temperature strength are generally well understood. While strength is a necessary characteristic, it is not the sole requirement for an alloy to perform useful engineering functions (Buckman, 1988).

Table 2.5 Properties comparison of pure refractory metals (Lambert, 1990)

Property	Niobium	Tantalan	**Molybdenum**	Tungsten	Rhenium
Structure and atomic properties					
Atomic number	41	73	**42**	74	75
Atomic weight	92.9064	180.95	**95.94**	183.85	186.31
Density at 20^0C (70^0F), g/cm^3(lb/in^3)	8.57 (0.310)	16.5 (0.600)	**10.22 (0.369)**	19.25 (0.695)	21.04 (0.760)
Crystal structure	bcc	Bcc	**Bcc**	bcc	hcp
Lattice constants, nm					
A	0.3294	0.3303	**0.3147**	0.3165	0.27609
C	…..	……	**……**	…….	0.45829
Slip plane at room temperature	110	110	**112**	……	0001-1010
Thermal properties					
Melting temperature, ^{0}C (^{0}F)	2468 (4474)	2996 (5425)	**2610 (4730)**	3410 (6170)	3180 (5755)
Boiling temperature, ^{0}C (^{0}F)	4927 (8901)	5427 (9801)	**5560 (10040)**	5700 (10290)	5760 (10400)
Vapor pressure at 2500K, mPa (torr)	5.3 (4x10^{-5})	0.11 (8x10^{-7})	**80 (6x10^{-4})**	0.0093 (7x10^{-8})	0.17(1.3x10^{-6})
Coefficent of expansion, near RT (a), µm/m K (µin/in. ^{0}F)	7.3 (4.1)	6.5 (3.6)	**4.9 (2.7)**	4.6 (2.6)	6.7 (3.7)
Specific heat at 20^0C (70^0F), kJ/kg (Btu/lb ^{0}F)	0.268 (0.0643)	0.139 (0.0333)	**0.276 (0.0662)**	0.138 (0.0331)	0.138 (0.0331)
Latent heat of fusion, kJ/kg K (Btu/lb)	290 (125)	145-174 (62-75)	**270 (115)**	220 (95)	177 (76)
Latent heat of vaporisation kJ/kg (Btu/lb)	7490 (3202)	4160-4270 (1790-1840)	**5123 (2160)**	4680 (2010)	3415 (1470)
Thermal coductivity, W/m.K(Btu/ft.h.^{0}F)					
At 20^0C (70^0F)	52.7 (30.4)	54.4 (31.4)	**142 (81.9)**	155 (89.4)	71 (41)
At 500^0C (930^0F)	63.2 (36.5)	66.6 (38.4)	**123 (71.0)**	130 (75)	……..
Electrical properties					
Elecrical conductivity at 18^0C (64^0F)	13.2	13.9	**33.0**	30.0	8.1
Electrical resistivity at 20^0C (70^0F), nΩ.m	160	135	**52**	53	193
Electrochemical eguivalent, mg/C	0.1926	0.375	**0.166**	0.318	0.276
Hall coefficent, nV.m/A.T	0.009	0.095	**……**	……	……
Magnetic properties					
Magnetic susceptibility (volume) at 25^0C (75^0F), mks system	28 x 10^{-6}	10.4 x 10^{-6}	**1.17 x 10^{-8}**	4.1 x 10^{-8}	0.37 x 10^{-6}
Optical properties					
Total emissivity at at 1500^0C (2730^0F), %	0.19	0.21	**0.19**	0.23	…….
Spectral emittance at λ=650 nm, %	0.37	0.49	**0.37**	0.43	……
Additional properties					
Poisson's ratio at 25^0C (75^0F)	0.38	0.35	**0.32**	0.28	0.49
Elastic modulus, GPa	103	185	**324**	400	469

(a) RT room temperature, (b) IACS, International Annealed Copper Standard

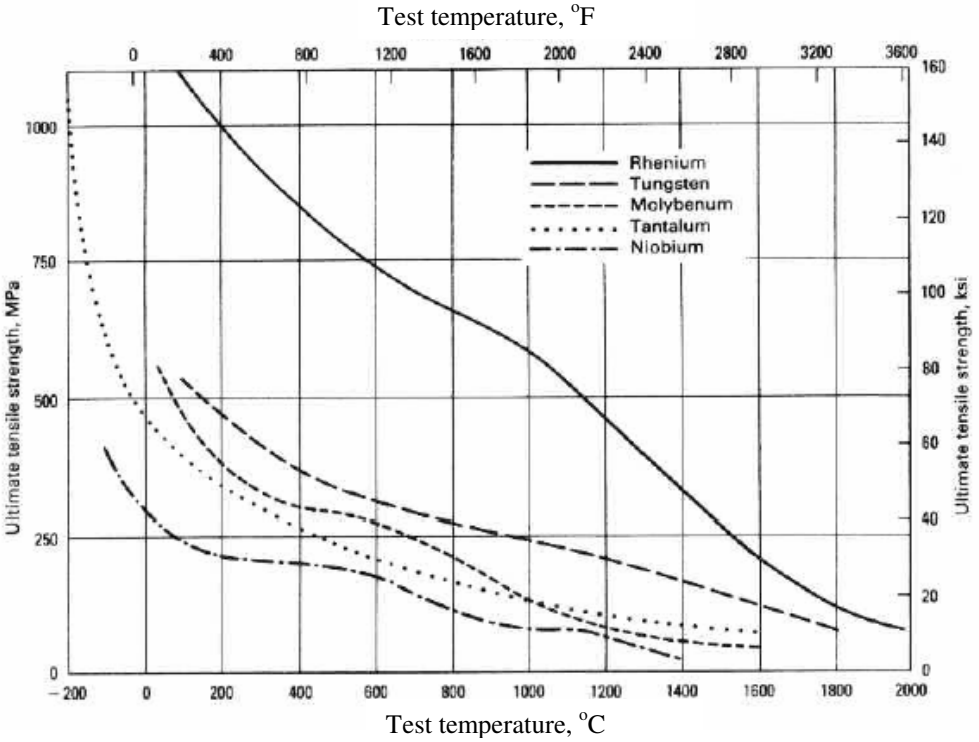

Figure 2.2 Test temperature vs. ultimate tensile strength of pure refractory metals (Lambert, 1990).

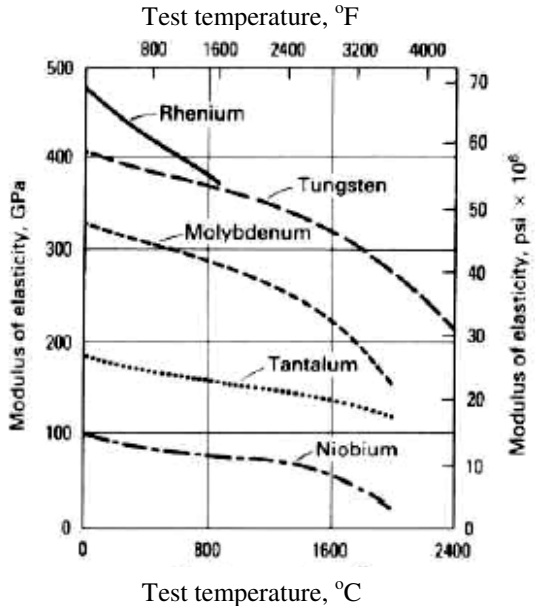

Figure 2.3 Test temperature vs. modulus of elasticity for pure refractory metals (Lambert, 1990).

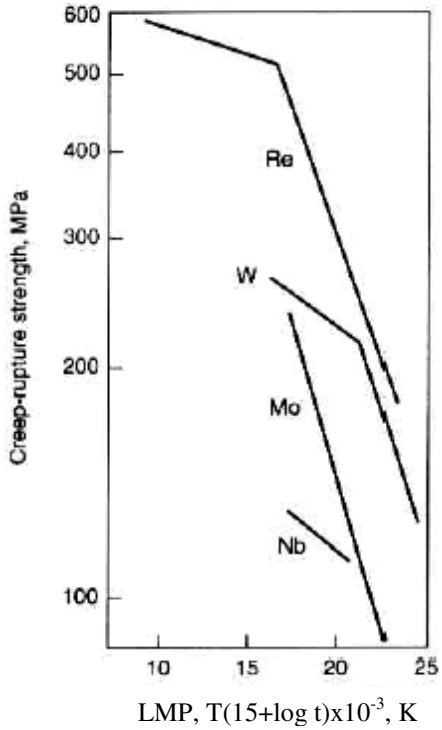

Figure 2.4 Creep rupture strenght for pure reftractory metals (Davis, 1997).

By defining refractory metals with respect to not only crystallography (bcc) and a melting point minimum (1925 ^{o}C) but also with respect to the ratio of oxide to metal melting temperature to that of the metal of less than one, then Nb, Ta, Mo and W emerge as the only elements that share this unique combination of features. (Table 2.6) The refractory metals under this defination all exhibit poor oxidation resistance and cannot be utilized in air at even at moderately elevated temperatures (Buckman,1988).

Table 2.6 Typical high temperature properties of pure refractory metal (Davis, 1997)

Pure Metal	Most common product form	Temperature, ^{o}C	Tensile, MPa	Temperature, ^{o}C	10h rupture, MPa
Niobium	All	1095	69	1095	37
Molybdenum	All	1000	50	980	175
Tantalum	All	1315	59	1315	7
Tungsten	Wrought bar	1000	620	…	…
	Sheet, wire	1650	120	1650	50
	CVD sheet	1000	565	….	…
Rhenium	All	20	1172/2324*	1600	56
		500	786/1196*	2200	21
		1000	588/855*	2800	4.2
		1500	262/276*	…	…
		2000	../103*	…	…
		2300	53/..*	…	…

* First value, annealed material; second value, wrought materials cold worked %15.

Since molybdenum and tungsten have a much lower solubility of oxygen than vanadium, niobium and tantalum, scaling can occur even at low oxygen pressures. However, at higher temperatures a quantitative description of oxidation rates is complicated by the high vaporization rate of MoO_3 or WO_3 (DiStefan, Pint, DeVan, 2000).

So refractory metals must be protected from oxidizing environments because of the relatively high temperatures of application, where they do not form protective

surface oxides. Nevertheless, their oxidation behavior in various environments and accompanying mechanical effects on their properties can be quite different.

Table 2.7 Comparison of melting points of metallic elements and their oxides (Buckman, 1988)

Element (stable crystal structure at room temperature)	Melting point, K		
	Metal	Oxide	Ro/m*
Ti (hcp)	1943	2098	1.1
Zr (hcp)	2125	2688	1.3
Hf (hcp)	2500	3173	1.3
V (bcc)	2175	963	0.4
Nb (bcc)	2740	1763	0.6
Ta (bcc)	3287	2045	0.6
Cr (bcc)	2130	2540	1.2
Mo (bcc)	2890	1068	0.4
W (bcc)	3680	1773	0.5
Re (hcp)	3453	570	0.2

*Ro/m=Tm(oxide)/Tm(metal)

2.4 Molybdenum-based Alloys

2.4.1 Molybdenum

Molybdenum has a body-centered cubic (bcc) crystal structure and displays the ductile to-brittle transition behavior typical of such metals. It combines a high melting point (2623°C) with strength retention at high temperatures (Helmik, 2003). Molybdenum is used as an alloying element in cast irons, steels, heat-resistant alloys to improve hardenability, toughness, abrasion resistance, corrosion resistance and strength and creep resistance at elevated temperatures. (Johnson, 1990). It also has high thermal conductivity, low coefficient of thermal expansion, and low specific heat providing resistance to thermal shock and fatigue (Helmik, 2003). Properties of pure molybdenum element is given in Table 2.5 shown above.

2.4.2 Corrosion Properties of Molybdenum

Molybdenum has particularly good resistance to corrosion by mineral acids, provided oxidizing agents are not present. It is also resistant to many liquid metals and to most molten glasses. In inert atmospheres, it is unaffected up to 1760^{o}C by refractory oxides. Molybdenum is relatively inert in hydrogen, ammonia and nitrogen up to about 1100^{o}C, but the superficial nitride case may be formed in ammonia or nitrogen (Johnson, 1990).

The primary disadvantage of molybdenum that prohibits its use in many high-temperature application is its rapid and catastrophic oxidation in air at temperature above roughly 790^{o}C. Oxidation produces molybdenum trioxide (MoO_3), which is very volatile and sublimes readily from the solid. Vaporization of the oxide prevents molybdenum from generating a protective film that would retard further oxidation. Oxidation can be promoted by melting as well as by vaporization of the oxides. MoO_3 melts at 795^{o}C, which is the oxide that is thought to form at the metal-oxide interface, forms a eutectic with MoO_3 that melts at 778^{o}C (Davis, 1997; Johnson, 1990).

Improvements in oxidation resistance depend on the development of improved coatings or new oxidation resistant alloys. Promising alloys have been identified in the Mo-Cr-Pd and Mo-W-Cr-Pd systems. Coating-development efforts also continue, although the pace of progress is slow. Incompatibility of thermal expansion coefficients between the coating and molybdenum substrate is an ongiong issue (Davis, 1997).

2.4.3 Types of Molybdenum-based Alloys

- Carbide-strengthened alloy; rely on the formation of fine reactive-metal carbides to dispersion strengthen the material, and to increase the recrystallization temperature above that of pure molybdenum by stabilizing the dislocation structure formed during processing.

- Solid-solution alloy; are produced in both VAC and P/M grades (Table 2.8).
- Combination alloys; contain both carbide-forming and substitutional elements to provide improved high-temperature strength.
- Dispersion-strengthened P/M alloys; rely on second-phase particles, introduced or produced during powder processing, to increase the resistance to recrystallized grain structure. These alloys have enchanced high temperature strength and improved low-temperature ductility (Davis, 1997).

Table 2.8 Composition of selected commercial molybdenum alloys (Davis, 1997)

Alloy	Alloying addition, wt%	Recrystallization temperature, ^{o}C
Unalloyed Mo	…	1100
Reactive-metal-carbide alloys		
TZM (MT–104)	0.5 Ti, 0.08 Zr, 0.03 C	1400
TZC	1.2 Ti, 0.3 Zr, 0.1 C	1550
MHC (HCM)	1.2 Hf, 0.05 C	1550
ZHM	0.5 Zr, 1.5 Hf, 0.2C	1550
Solid-solution alloys		
25 W	25 W	1200
30 W	30 W	1200
5 Re	5 Re	1200
41 Re	41 Re	1300
50 Re	50 Re	1300
Combination alloy		
HWM–25 (Mo-25WH)	1 Hf, 0.07 C, 25 W	1650
Dispersion-strengthened alloys		
Z–6	0.5 ZrO2	1250
MH (HD)	150 K, 300 Si (ppm)	1800
KW	200 K, 300 Si, 100 Al (ppm)	1800

2.4.4 Applications of Molybdenum-based Alloys

Due to combination of these properties and characteristics mentioned above, applications of molybdenum and its alloys are summarized below;

- In electrical and electronic industries;
    - cathodes, cathode supports for radar devices, current leads for cathodes, magnetron end hats, mandrels for winding tungsten filaments,
    - resistance heating elements are used in electric furnaces that operate at temperatures up to 2205^{o}C,
- In the missile industries;
    - high temperature parts such as nozzles, leading edges of control surfaces, support vanes, struts, reentry cones, heat-radiation shields, heat sinks, turbine wheels and pumps,
    - in airframes, in many aerospace application,
- In the metalworking industries;
    - die casting cores,
    - for hot work tools such as pierce points and extrusion and isothermal forging dies, for boring bars, tool shanks and chill plates and for tips on resistance welding electrodes,
    - also for cladding, for molds and for thermocouples,
- In the metallizing industries,
- In nuclear industry,
- In glass industry,
- In the lighting industry;
    - for feed-trough wires for halogen bulbs,
    - as die-casting cores in the semiconductor industry (Gritsch & et. al., 2000; Sharma, Chakraborty & Suri, 2004).

CHAPTER THREE
HIGH TEMPERATURE CORROSION

3.1 High Temperature Corrosion

High temperature corrosion plays an important role in the selection of materials for construction of industrial equipment. The principle modes of high temperature corrosion frequently responsible for equipment problems are oxidation, carburization and metal dusting, nitridation, halogen corrosion, sulfidation, ash/salt deposit corrosion, molten salt corrosion, molten metal corrosion are summarized schematically in Fig. 3.1 (Lai, 1990a).

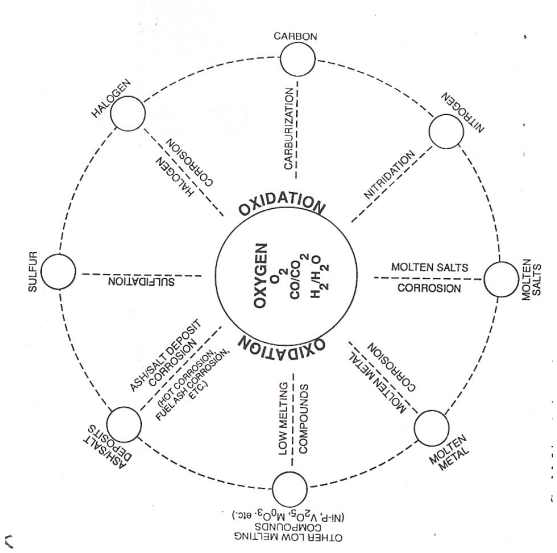

Figure 3.1 Schematic showing the principal modes of high temperature corrosion in industrial environments (Lai, 1990a).

When metal is exposed to an oxidizing gas at elevated temperatures, corrosion can occur by direct reaction with the gas, without the need for presence of a liquid electrolyte. This type of corrosion is reffered to as tarnishing, high temperature oxidation or scaling. The rate of attack increases substantially with temperature. The surface film typically thickens as a result of reaction at scale/gas or metal/scale interface due to cation or anion transport through the scale, which behaves as a solid

electrolyte. For continous nonporous scales, ionic transport trough the scale is the rate-controlling process. The thermodynamic stability, the ionic defect structure, and certain morphological features of the scale formed are key factors in determining the resistance of an alloy to a specific environment (Wright, 1987).

Thermodynamically, an oxide is likely to form on a metal surface when the oxygen potential in the environment is greater than the oxygen partial pressure in equilibrium with the oxide. The oxygen partial pressure (P_{O2}^{eqm}) in equilibrium with the oxide can be determined from the standard free energy of formation of the oxide (ΔG^o) (Lai, 1990b).

The following equilibrium relations show how these values related to each other:

$M + O_2 = MO_2$; where M is metal (3.1)

$\Delta G^o = -RT \ln(a_{MO2}/a_M.P_{O2})$ (3.2)

a= activity, T= Temperature, R= gas constant

$\Delta G^o = RT \ln P_{O2}$ (3.3)

$P_{O2}^{eqm} = e^{\Delta G/RT}$ (3.4)

The affinities of metals for oxygen are usually presented in the form of an Ellingham Diagram (Fig.3.2), in which the standard Gibbs energy of oxide formation (per mole of oxygen) is plotted against temperature.

Initial product film growth over a metal is usually very rapid. If the scale is a nonporous solid and completely covers the metal surface, the reaction rate will decrease when the thickness reaches a few thousand Angstroms as transport of reactive species through the film becomes rate controlling. The subsequent corrosion rate depends on the details of this transport mechanism, which may be due to electrical potential or concentration gradients or to migration along preferential paths

and so may correspond to any of several rate laws. Where a diffusion process is rate controlling, the kinetics usually follow a parabolic rate law, in which the rate progressively decreases with time. If the scale is porous or does not completely cover the metal surface, a linear rate is usually observed (Wright, 1987).

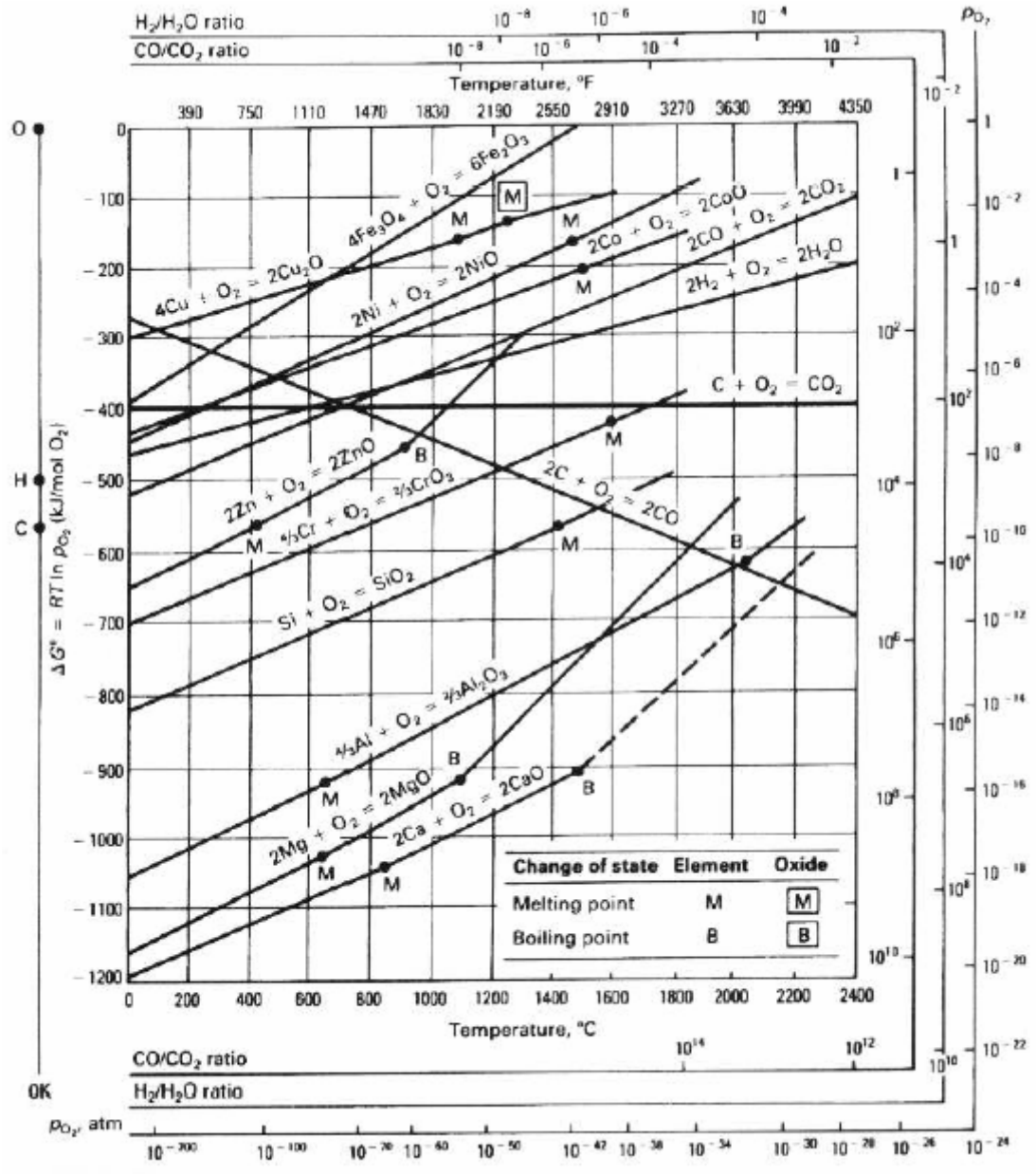

Figure 3.2 Ellingham Diagram (Lai, 1990b).

The desired characteristic for a protective oxide scale include the following:

- High thermodynamic stability (high negative Gibbs free energy of formation) so that it forms preferentially to other possible reaction products,
- Low vapor pressure so that the oxide forms as a solid and does not react further with the environment to form volatile products, does not evaporate into the atmosphere,
- Pilling-Bedwoth ratio greater than 1.0 so that the oxide completely covers the metal surface,
- Low coeffient of diffusion of reactant species (metal cations and corrodent anions) so that the scale has a slow growth rate,
- High melting temperature,
- Good adherence to the metal substrate, which usullly involves a coefficient of thermal expansion close to that of the metal, and sufficient high temperature plasticity to resist fracture from differential thermal expansion stress,
- Free of pores, cracks, or other defects thereby preventing short circuit transport of reactants across it (Stott, 1989; Wright, 1987).

3.2 Cyclic Oxidation of High-Temperature Alloys

Oxide scales have generally lower coefficient of thermal expansion than the metallic substrates on which they grow. During a temperature variation, this dilatation difference induces thermal stresses which, added to the growth stresses, can cause the cracking and eventual spallation of the scale. Under very high stresses or low temperature, which are conditions likely to occur during cyclic oxidation, the stresses can be relieved by scale cracking or buckling, depending on the respective scale and scale/metal interfacial strength. These phenomeno can lead to partial scale spallation and, as a result, an unprotected substrate area is exposed to the oxidizing environment. Repetition of this sequence eventually leads to the formation of non-protective scales and therefore accelerated degradation rates (Mevrel, 1987).

3.3 High Temperature Oxidation of Nickel-base Alloys

3.3.1 Pure Nickel

Pure nickel oxidizes according to a parabolic rate equation such as :

$$w^2=K_p\,t \tag{3.5}$$

Here,
w: weight gain (or scale thickness)
t: time
and K_p: parabolic rate constant

The oxide formed is NiO and at elevated temperatures a relatively coarse columnar-grained compact oxide layer develops over high purity material. Under some circumstances a two-layer scale develop; the outer layer has the same coarse-grained compact apperance and closer to the metal- a fine-grained porous layer appears. The development of this two layer structure seems to be encouraged by the presence of small amounts of impurity (Wallwork, 1975).

3.3.2 Nickel %10–15 Cr Alloys

The addition of small amount of chromium to nickel increases the rate of oxidation (Fig.3.3) which is attributed to a Wagner-Hauffe mechanism with chromium dissolving in the p-type NiO and increasing the concentration of mobile cation vacancies, although the solubility of Cr^{3+} in NiO is fairly restricted. A two layer scale develops with the inner fine-grained layer containing small particles of the spinel $NiCr_2O_4$ in an NiO matrix; in addition, some of the chromium is oxidized internally within the metal.

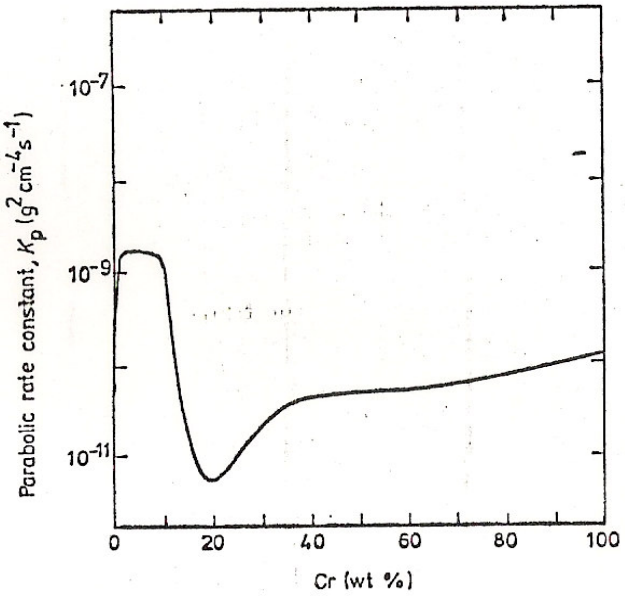

Figure 3.3 Variation of the parabolic rate constant with alloy composition for Ni-Cr alloys at 1000°C in oxygen at 760 Torr (Wallwork, 1975).

Because both NiO and Cr_2O_3 are stable oxides in 1 atm oxygen, various factors, particularly thermodynamics and kinetics influence the overall scale development. Chromium has a higher affinity for oxygen than nickel and forms a more stable oxide while NiO is a less stoichiometric oxide than Cr_2O_3 and thickens at a considerably faster than Cr_2O_3. Hence, although the relative free energies of formation of the oxides predict the thermodynamically favoured oxide, they do not determine completely the nature of transient oxide or of the steady state scale. The alloy chromium content mainly determines whether Cr_2O_3 develops as an external scale or as internal oxide precipitates in the alloy lattice. If the alloy contained less than about 10 % Cr, there is usually insufficient Cr for an external scale and internal Cr_2O_3 is formed. At increased chromium concentrations, development of an external layer of Cr_2O_3 occurs eventually. This is facilitated by a high alloy chromium content, a high alloy interdiffusion coefficient, which ensures rapid replenishment of chromium as it is taken into the scale, and low oxygen solubility and diffusivity in the alloy, which enables chromium to diffuse to the surface without being oxidised to form internal precipitates (Sttot, 1989).

3.3.3 Nickel %15–20 Cr Alloys

Fig. 3.4 shows a schematic represantation of oxidation of Ni-20 Cr in the left hand sequence and oxidation of Ni-5Cr in the right hand sequence. The observed transition to the formation of an external Cr_2O_3 scale takes place between 15 and 20 wt % Cr but the Cr_2O_3 layer does not develop at once. In the initial stages, nuclei of all the stable oxide phases, NiO, Cr_2O_3 and $NiCr_2O_4$, form in the surface. Due to its defect state, the NiO grows more rapidly and envelops the Cr_2O_3. Because NiO is less stable than Cr_2O_3, it supplies oxygen at its dissociation pressure which is at a sufficiently high potential to react with chromium to produce Cr_2O_3 at, or near , the scale/alloy interface (Stott, 1989; Wright, 1987).

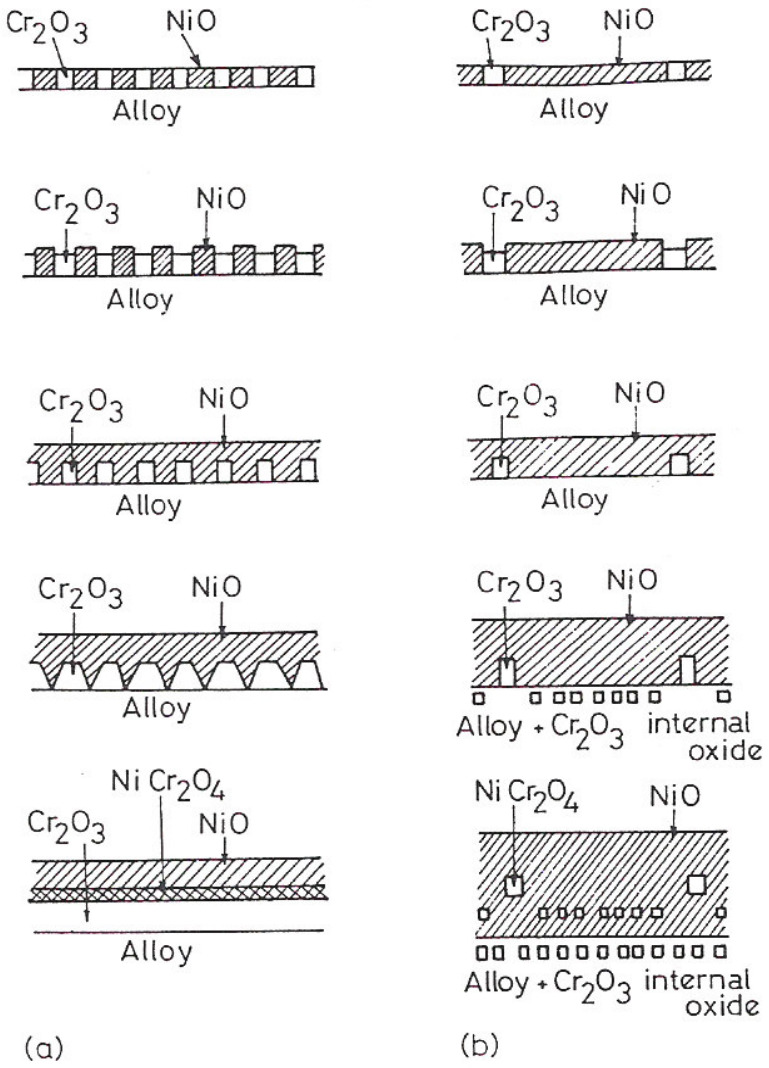

Figure 3.4 Schematic oxidation of (a) Cr-rich and (b) Cr-lean alloys (Wood & Sttot, 1987).

Eventually, a complete healing layer of this oxide is established. The final steady state scale is an outer duplex layer of NiO consisting of an outer compact region and an inner more porous region, incorparating $NiCr_2O_4$ precipitates, and an inner healing Cr_2O_3 layer (Sttot, 1987,1989).

A solid state reaction occurs as shown during the oxidation:

$$NiO\ (s)+Cr_2O_3\ (s)= NiCr_2O_4\ (s) \qquad (3.6)$$

by which a spinel phase is formed within the scale.

This is achieved with Ni-(20 or 40) Cr but not Ni-5Cr, where internal oxide grows progressively into the alloy. Now $NiCr_2O_4$ can also participate in the reaction, forming a layer between the NiO and Cr_2O_3 in the Ni-(20 or 40) Cr alloy and particles in the iner NiO layer in the Ni-5Cr alloy. The steady state scale is essentially the thermodynamically favoured Cr_2O_3 for Ni-Cr-(20 or 40) Cr, but is essentially NiO for Ni-5Cr. At lower oxygen potentials, a complete Cr_2O_3 layer develops earlier (Wood& Stott, 1987).

3.4 Oxidation of Molybdenum

The end product of oxidation of molybdenum at high temperatures and relatively high oxygen partial pressures is well known to be MoO_3, which has a melting temperature of 794°C and is decidedly volatile at temperatures as low as 700°C. The kinetics of oxidation of a metal that forms a volatile oxide is usually described using a paralinear relationship between weight change and time. One such metal is chromium. In the case of chromium oxidation, chromium oxide is formed with parabolic kinetics while it vaporizes with linear kinetics. A steady state oxide thickness is formed while the metal recesses in a linear fashion.

Studies on molybdenum at lower temperatures in high levels of oxygen showed the following:

1. parabolic rate law at 250-450^{0}C,
2. linear behavior above 400^{0}C,
3. the role of MoO_2 and other oxides (MoO_Z), where 2>Z>3 between 450^{o}C and 650^{o}C),
4. high vaporization of MoO_3, mass loss and oxidation rates above 650^{o}C (Smolik, Petti &Schuetz, 2003).

Molybdenum oxide is volatile, similar to chromium oxide, but at high temperatures (i.e. above ~800°C) the oxide vaporizes as soon as it is formed because of its high vapor pressure. Therefore, a steady state oxide thickness is never formed. As a result of this rapid volatilization, other factors aside from the obvious temperature and oxygen partial pressure effects, heavily contribute to the oxidation kinetics of molybdenum at high temperatures.

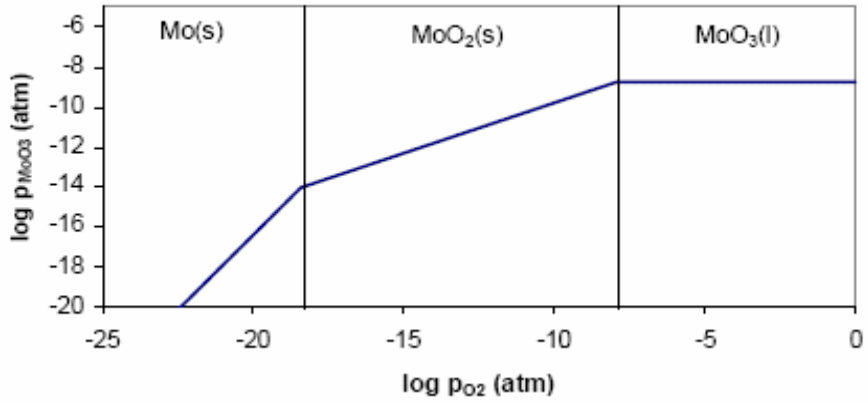

Figure 3.5 Volatile species diagram for molybdenum at 1100K (Helmick, 2003).

Fig.3.5 shows a volatile species diagram for molybdenum at 1100K (827°C). The diagram shows how the vapor pressure of MoO_3 varies with oxygen pressure as well as the oxygen pressure required to oxidize Mo to MoO_2 using the following reaction.

$$Mo(s) + O_2(g) \rightarrow MoO_2(s) \qquad (3.7)$$

and the oxygen pressure required to further oxidize MoO_2 to MoO_3 using the following reaction:

$$MoO_2(s) + 1/2O_2(g) \rightarrow MoO_3(l) \quad (3.8)$$

The reaction used to calculate the pressure of $MoO_3(g)$ over the Mo(s) condensed phase is:

$$Mo(s) + 3/2O_2(g) \rightarrow MoO_3(g) \quad (3.9)$$

and over the $MoO_2(s)$ condensed phase is:

$$MoO_2(s) + 1/2O_2(g) \rightarrow MoO_3(g) \quad (3.10)$$

and over the $MoO_3(l)$ condensed phase is:

$$MoO_3(l) \rightarrow MoO_3(g) \quad (3.11)$$

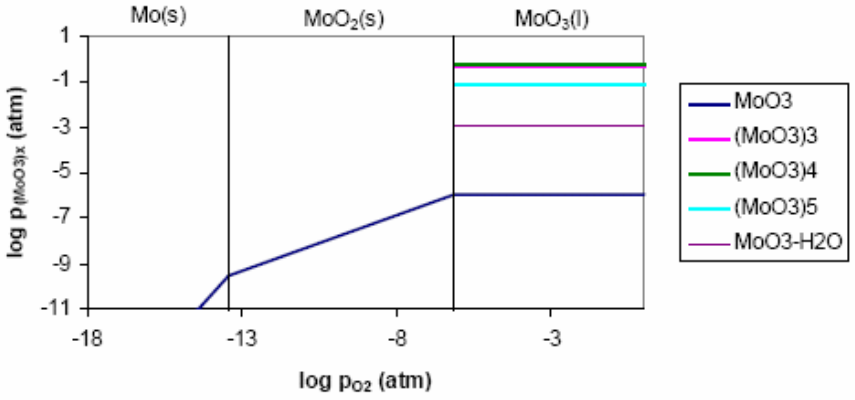

Figure 3.6 Volatile species diagram for molybdenum at 1350K (p_{H2O} = 0.1atm) (Helmick, 2003).

Fig.3.6 is a volatile species diagram for molybdenum at 1350K (1077°C).This diagram, once again, shows how the vapor pressure of the vapor species vary with oxygen pressure. The oxygen pressures required to oxidize Mo(s) to $MoO_2(s)$ and

MoO_2(s) to MoO_3(l) are calculated using (3.7) and (3.8), respectively. The vapor pressures of MoO_3(g) over the three condensed phases are calculated using reactions (3.9), (3.10) and (3.11). In addition, the vapor pressure of several polymers of MoO_3 and a hydrated molybdenum oxide over the condensed phase MoO_3(l) were plotted on the diagram (calculated at a water vapor pressure of 0.1atm). The reactions used to calculate the vapor pressures of the three polymers of MoO_3 on the diagram are as follows:

$$3MoO_3\,(l) \rightarrow (MoO_3)_3(g) \tag{3.12}$$

$$4MoO_3\,(l) \rightarrow (MoO_3)_4(g) \tag{3.13}$$

$$5MoO_3\,(l) \rightarrow (MoO_3)_5(g) \tag{3.14}$$

and the reaction used to calculate the vapor pressure of the hydrated molybdenum oxide on the diagram is:

$$MoO_3\,(l) + H_2O(g) \rightarrow MoO_3{\bullet}H_2O(g) \tag{3.15}$$

At 1350K, the vapor species that have the highest vapor pressures are $(MoO_3)_3$ and $(MoO_3)_4$ both of which have vapor pressure of ~0.5atm. Since MoO_3 vaporizes as soon as it is formed at high temperatures, an atmosphere rich in MoO_3(g) is formed near the surface of the metal. If the partial pressure of the MoO_3(g) reaches its saturation pressure, condensed MoO_3 can form on the surface. This means that the partial pressure of MoO_3(g) can control the transport mechanism for oxidation. If the MoO_3(g) is permitted to reach its saturation pressure then the transport mechanism will be condensed phase diffusion through the oxide layer on the surface of the metal barring any cracks and pores in the scale. On the other hand, if the partial pressure of MoO_3(g) remains below the saturation pressure, the transport mechanism will be gas phase diffusion near the surface of the metal.

By controlling the partial pressure of MoO_3(g) near the surface of the metal, the rate of volatilization of MoO_3 from the surface will be controlled. The controlled partial pressure of MoO_3(g) by varying the flow rate of air passed the molybdenum specimen. They concluded that rapid gas flow rate increased the volatilization of MoO_3, which in turn increased the oxidation rate. Also, they suggested that there is a maximum oxidation rate for molybdenum at a given temperature at which the partial pressure of MoO_3(g) is maintained at a low value near the surface of the specimen. These results suggest that the description of oxidation of molybdenum includes boundary layer flow kinetics controlling the transport mechanisms (Helmick, 2003, p.21-23).

3.5 Effects of Mo on Corrosion of Ni-Cr base Alloys

X-ray diffraction taken from study of Mizutani (1990) showed that NiO, $NiCr_2O_4$ and Cr_2O_3 formed on the surface of the Ni-Cr binary alloys whose composition of Cr ranged from 5 to 25 wt%, whereas NiO and $NiCr_2O_4$ rarely formed on the Ni-Cr binary alloys whose composition of Cr ranged from 30 to 40 wt%. This suggests that the formation of Cr_2O_3 prevents the formation of NiO on the alloy with a high Cr content. The weight gain of the Ni-Cr-Mo ternary alloys was smaller than that of the Ni-Cr binary alloys without Mo, and the temperature effects on the weight gain of the Ni-Cr-Mo ternary alloys were different for each Cr content. However, the effect of the amounts of Mo was small. NiO, $NiCr_2O_4$, Cr_2O_3 and MoO_2 were identified by X-ray diffraction on the surface of the Ni-Cr-Mo ternary alloys. According to the SEM observation, it seems that NiO was formed at the outermost layer, both $NiCr_2O_4$ and Cr_2O_3 at the inside layer, and MoO_2 at the innermost layer. The formation of both NiO and Cr_2O_3 on the Ni-Cr-Mo ternary alloys was restrained compared with that of the Ni-Cr binary alloys. However, the adhesion of oxides to the Ni-Cr-Mo ternary alloys was lower than that of the Ni-Cr binary alloys.

CHAPTER FOUR
SCANNING ELECTRON MICROSCOPE (SEM)

4.1 Scanning Electron Microscope (SEM)

Scanning electron microscope is one of the most important instrument for investigating the microstructure of metallic materials. Primary use of the scanning electron microscope is to produce high-resolution and depth-of-field images of sample surfaces. A second use is to provide chemical analyses of micron-sized areas of the structure revealed on these surfaces. Additional to image formation and microchemical analysis, the scanning electron microscope provides some other functions. These are; (1) the use of channeling patterns to evaluate the crystallographic orientation of micron-sized region, (2) the use of backscattered detectors to reveal grain boundaries on unetched samples and domain boundaries in ferromagnetic alloys, (3) the use of voltage contrast, electron beam induced current and cathodoluminescence for such purposes as characterization and failure analysis of semiconductor devices. The principal features of the scanning electron microscope are shown in Fig. 4.1 (Verhoeven, 1986).

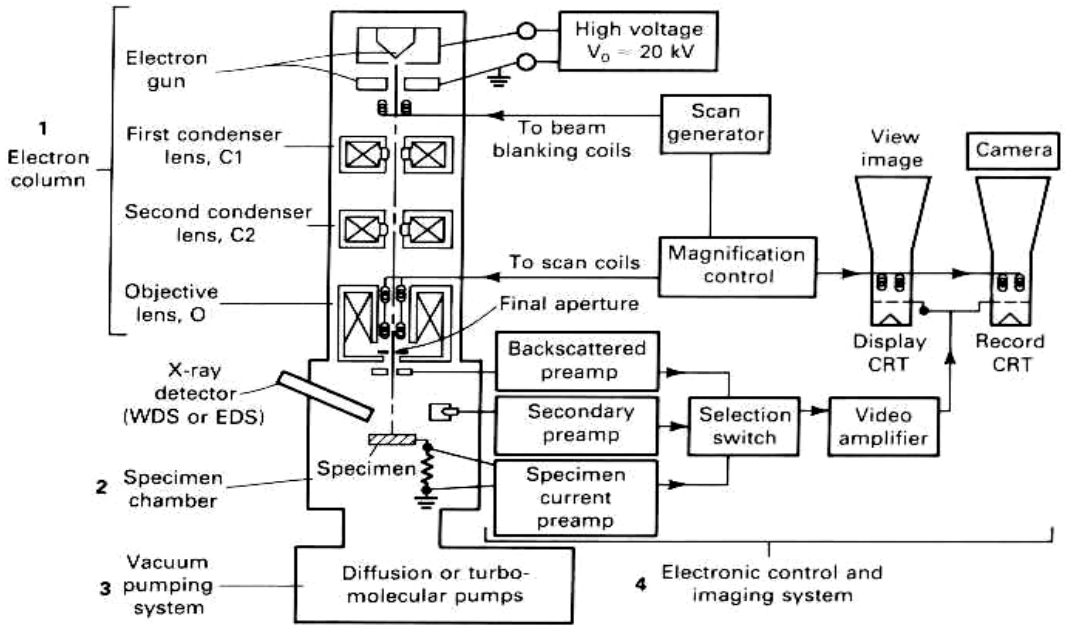

Figure 4.1 Basic components of the scanning electron microscope (WDS :Wawelength dispersive spectrometer, EDS: Energy dispersive spectrometer, CRT: Cathode-ray tube) (Verhoeven, 1986).

4.2 Signals Generated by the Scanning Electron Beam

When an electron beam strikes a solid surface, electrons and x-rays are emitted from the surface. The energy distribution of these signals is shown qualitatively in Fig. 4.2. In addition to secondary electron detector (which can also be used to detect backscattered detectors), most scanning electron microscopes are equipped with an x-ray detector, and specialized backscattered detectors. Some types of signals and supplies information on the region close to the surface from which information is obtained are shown in Fig 4.3 (Exner, 1985; Verhoeven, 1986)

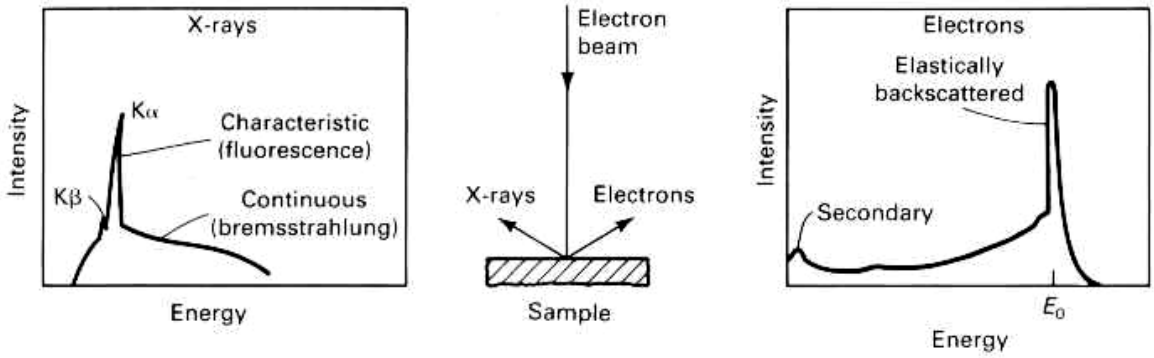

Figure 4.2 Energy distribution of signals generated by the electron beam (Verhoeven, 1986).

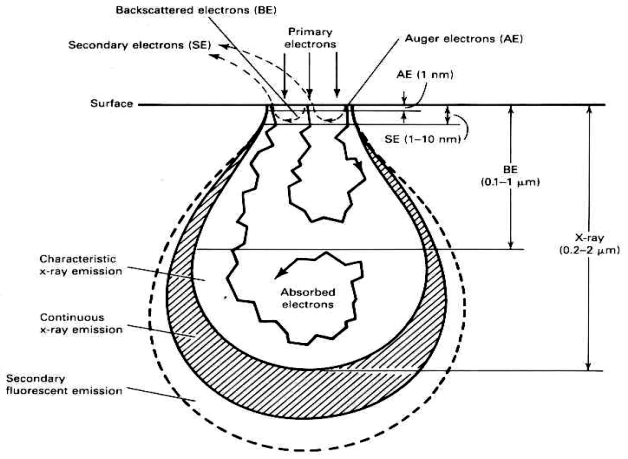

Figure 4.3 Types of electron beam-excited electrons and radiation used in SEM and depth of the region below the specimen surface from which information is obtained (Exner, 1985).

The electron generated by the electron beam can be divided into three types; secondary, auger and backscattered (Fig 4.4) The backsttered electrons may be further divided into three types so that the emitted electron distribution becomes:

- Backscattered electrons;

Type 1 Elastically scattered,

Type 2 Plasmon and interband transition scattered,

Type 3 Inelastically scattered ,

- Auger electrons,
- Secondary electrons,

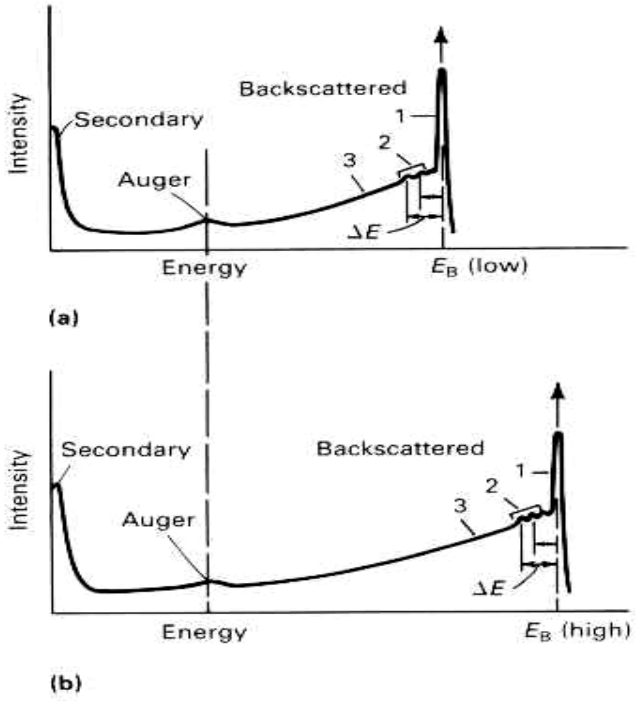

Figure 4.4 The energy distribution of emitted electrons at (a) low beam energy (around 1 keV) and (b) a higher beam energy (around 5 keV) (Verhoeven, 1986).

4.2.1 Backscattered Electrons (BE)

After incident electrons are scattered within the specimen some of them are backscattered while keeping a relatively high energy and emitted again from the specimen surface. These electrons are termed backscattered electrons. The energy distribution of backscattered electrons depend on the primary energy of incident electrons, the number of outer-shell electrons, the atomic number of the material and

the surface inclination of the specimen. As the atomic number of material hit by the incident beam decreases, fewer electrons are backscattered, and more energy is lost. In materials with high atomic number, many electrons are backscattered by atoms close to the surface, with little change in energy. So, energy spectrum and depth of escape of backscattered electrons are directly related to the atomic number of the materials (Exner, 1985; Jeol, 2006).

There are three processes that can scattered an electron back out from the surface, as listed above. Elastically scattered electrons emerge with essentially the same energy as the beam energy. E_B; inelastically scattered electrons generally undergo many scattering interactions and emerge with a spectrum of energies lower than the beam energy. The type 2 electrons are scattered by intersections that produce a plasmon oscillation of the electrons in the sample material or a transition of sample electrons between different energy bands (Verhoeven, 1986).

4.2.2 Secondary Electrons (SE)

Secondary electrons generally display a peak intensity at approximately only 5 eV (Fig. 4.4). These electrons are the signal used to generate high- resolution images in the scanning electron microscope. They can generated by the primary electron beam or any scattered electron that passes near the surface. Comparison of Fig. 4.4 (a) and Fig. 4.4 (b) illustrates that the energies of the secondary and auger electrons are fixed, but the backscattered electrons shift their energy values as the primary beam energy is changed (Verhoeven, 1986).

4.2.3 Characteristic X-rays and Auger Electrons

Characteristic x-rays are generated as a result of the incoming electrons knocking out intershell electrons (K, L, M, depending on atomic number) from atoms near the surface. After a K electron is knocked out, the surface atoms emits either a characteristic x-ray or an auger electron. The probability for auger emission exceeds

that for x-ray emission as atomic number decreases. As with the characteristic x-ray emission, the energy of auger electrons is different for each element.

X-rays excited by the electron beam form two types of spectra : (1) the bremsstrahlung (electromagnetic radiation emitted by electrons when they pass through matter) with a continuous spectrum and (2) the characteristic radiation with a distinct line spectrum. The line spectrum can be analyzed by wavelength-dispersive spectrometry (WDS), which is used nearly exclusively with devoted electron probe microanalyzrs and by energy dispersive spectrometry (EDS) (Exner,1985; Verhoeven, 1986).

CHAPTER FIVE
EXPERIMENTAL STUDIES

5.1 Aim of Study

In this study, oxidation behavior of two nickel-base alloys (C-22 and C-276) containing more than %10 Mo was investigated to observe and gain an understanding on the behavior of refractory metals.

Oxidation tests were divided into three groups according to the preparation of sample and oxidation time. Group 2 tests are also divided into two groups, **low ($T<1000^oC$)** and **high ($T>1000^oC$)** temperature oxidation tests according to test temperature.

5.2 Materials Used and Sample Preparation for Oxidation Tests

Alloy samples used in this work were produced by Daido Steel Co Ltd (Japan). Nominal compositions of these alloys are given in Table 5.1. Of these alloys, the C-22 alloy has a Cr content of more than 20%. However the Mo content of this alloy was slightly lower than that of the alloy C-276.

Table 5.1 Nominal compositions of the studied Ni-base alloys (Stoloff N.S., 1990)

Alloys	Composition, weight %									
	Ni	Cr	Co	Mo	W	Fe	Mn	Si	C	Other
C-276	Balance	15.5	2.5	16.0	3.7	5.5	1.0	0.1	0.03	0.3V
C-22	Balance	21.5	2.5	13.5	4.0	5.5	1.0	0.1	0.01	0.3V

For oxidation tests, about 2mm thick, disc-shaped samples were cut from cylindrical mill products. A small hole (2mm in diameter) was drilled close to the sample circumference to suspend the sample inside a ceramic crucible using a Ni-Cr resistance wire. Before exposure to the test environment, two large surfaces of all samples were prepared for oxidation tests, differently, for each test group as follows;

- Preparation of samples for microstructure investigation: Surfaces of test samples were ground up to 1200 grit SiC-based grinding paper and then polished using diamond slurry with an average diameter of 1 µm.

- Preparation of **GROUP 1** test samples: For this test group, purpose of the investigation was to observe the effect of surface roughness on oxidation behavior. Thus, two samples of only the C-276 alloy were prepared for the test. One of the C-276 sample surfaces were ground up to 1200 grit SiC paper and then polished using on alumina slurry. The other test sample was ground up to 800 grit SiC paper.

- Preparation of **GROUP 2** and **GROUP 3** test samples: The purpose of these facts was to investigate the oxidation behavior of test alloys using samples with similar surface preparation. Thus for these test, surfaces of C-22 and C-276 alloy samples were ground up to 800 grit SiC paper.

After surface preparation, samples in all groups were cleaned, ultrasonically, in acetone then dried quickly in flowing warm air and weighed using a balance with 0.1mg sensitivity.

5.3 Oxidation Tests

Oxidation tests were performed in a box furnace (HERAEUS-Baseloader BL 1801Model) (Fig. 5.1). After placing a single sample of alloy inside a crucible, two crucibles were placed inside the furnace side by side and heated to the test temperature. Tests were conducted under the stagnant air environment of the furnace. Details of the test procedures followed for each group are explained below.

Figure 5.1 High temperature furnace

- In **GROUP 1** test, samples were heated to 1150^{o}C in furnace atmosphere and kept at this temperature for 6 hours before cooling to room temperature in the furnace.

- In **GROUP 2** tests; samples were heated to 500^{o}C and kept at this temperature for 30 minutes before cooling to room temperature in the furnace. A similar process of heating and cooling was repeated for the same samples starting at 700^{o}C, 800^{o}C, 900^{o}C and 1150^{o}C after the same holding time. After each cycle, samples and spalled oxide scales were weighed. Samples surfaces were also examined using SEM and EDS.

- In **GROUP 3** tests; samples were heated to 1150^{o}C under the air environment of the furnace. Samples were kept at this temperature for 6 hours before cooling to room temperature in the furnace. A similar cycle of heating and cooling was repeated 7 times for a total of 42 hours. After each cycle, crucibles and samples were examined visually without removing them from the furnace.

5.4 Mass Change Measurements of Test Samples

The most frequently used method for determining alloy performance in a corrosive environment is to measure sample mass change as a result of corrosion. This is done by measuring the difference in sample weight following the test and dividing this by the specimen total surface area as measured of the beginning of the test.

To measure mass changes, at the end of the tests, samples were carefully removed from crucibles to prevent accidental spalling of corrosion products from sample surfaces. Corrosion products spalled from samples into crucibles during testing were collected as much as possible and weighed after each test. Mass chance results per unit area of each sample were reported in the form of tables.

5.5 Characterization Techniques Used for Corrosion Products

5.5.1 SEM and EDS

The microstructure investigations for samples and their corrosion products were done by a scanning electron microscope (Jeol-JSM 6060 SEM) equipped with an energy dispersive X-ray spectroscopy (IXRF System EDS) system after and before oxidation tests. (Fig. 5.2 a) Accelerating voltages of 25 and 20 kV were used for imaging and SEM/ EDX analyses, respectively. These tests were also used to investigate inner surfaces of crucibles used in the tests. Beside the outermost surfaces, sectioned surfaces of some selected samples were also examined by SEM/EDS. For this, samples were mounted in polyster sectioned, ground up to 1200 grit and then polished using 1 µm diamond slurry.

(a) (b)

Figure 5.2 Photographs of (a) scanning electron microscope (SEM) and (b) X-ray diffractometer (XRD) used for characterization.

The SEM used also had a capability of producing images using back scattered electrons (BE). Because this mode of imaging derives its contrast from atomic number differences of elements in the imaged area, distribution of heavy elements like Mo in the developed microstructures was able to be distinguished easily from most of the other alloying elements.

5.5.2 XRD

Analyses of the crystalline corrosion product phases in the scales formed on bulk samples and spalled oxide scales were performed using Rigaku Model X-ray diffractometer (Fig. 5.2b) with CuKα radiation. The 2θ angular scans were performed within the range of 3-90^{o} with a step size of 0.02^{o} and counting, at each step duration of 4s.

CHAPTER SIX
EXPERIMENTAL RESULTS AND DISCUSSION

6.1 SEM Images and EDS Analyses of Samples before Oxidation Tests

SEM micrographs in Fig. 6.1 a and b show surface appearances of C-276 and C-22 alloy samples before oxidation tests. EDS analyses of samples are given in Table 6.1. When analyses results are compared with the nominal composition reported for these alloys (Table 5.1), it is observed that Cr amounts measured in alloys were in agreement with the reported values whereas the measured Mo amounts were approximately %3 lower than the nominal values.

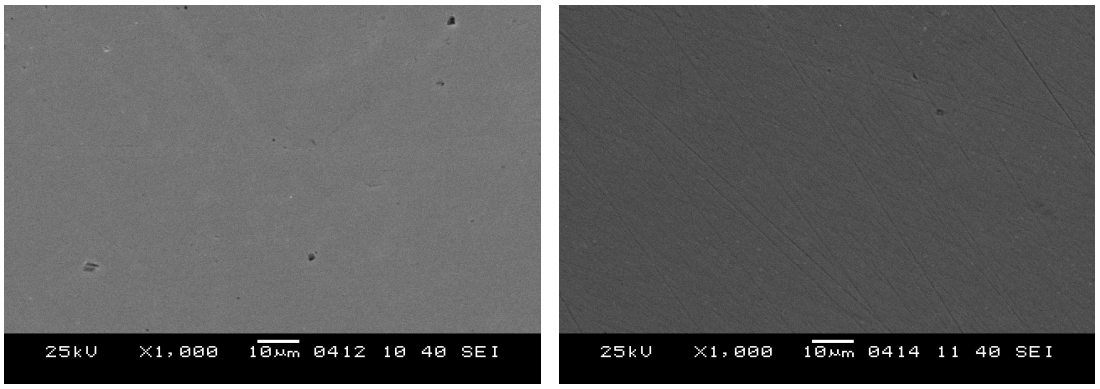

(a) (b)

Figure 6.1 SEM micrographs of (a) C-276 and (b) C-22 alloy sample surfaces before oxidation tests.

Table 6.1 Average values of 4 EDS analyses of samples before oxidation test

Alloys	Concentration , wt %				
	Cr	Mo	Fe	W	Ni
C-276	15.0	13.5	5.6	6.2	58.0
C–22	20.4	11.2	5.1	5.38	55.8

6.2 Results and Discussion for Group 1 Tests

6.2.1 Mass Changes

Mass changes of the alloy samples after oxidation tests are shown in Table 6.2. Mass gains were observed for both samples after the test. For the alumina polished C-276

sample, the mass gain per unit surface area was higher. Although it was difficult to collect all of the scale pieces inside the crucibles, approximate amounts of scale collected were 0.0049 g for the 800 grit ground C-276 sample and 0.002 g for the alumina polished C-276 sample.

Table 6.2 Mass changes of alloy samples after Group 1 oxidation test

Samples	Before oxidation test (W1) g	After oxidation test (W2) g	Mass Change (ΔW=W2-W1) g	Mass change / surface area g/cm^2
C-276 (800 grit ground sample)	1.5258	1.5270*	0.0012	0.0005
C-276 (polished sample)	1.5483	1.5509*	0.0026	0.0011

*Spalled oxide scale is observed after oxidation test. The values are total mass of oxidized sample and spalled oxide scales from their surface.

6.2.2 SEM Images and EDS Analyses of Samples after Oxidation Test

Spallation area from the polished surface after oxidation test at 1150°C/6 h is given in Fig. 6.2 a. Same spallation areas are also observed on 800 grit ground C-276 surface. Fig 6.2 b and c shows oxide scales formed during the oxidation test. Dark and large grains are Ni-rich, however small and bright grains seen in Fig. 6.2 b are both Ni and Cr rich oxides (Table 6.3).

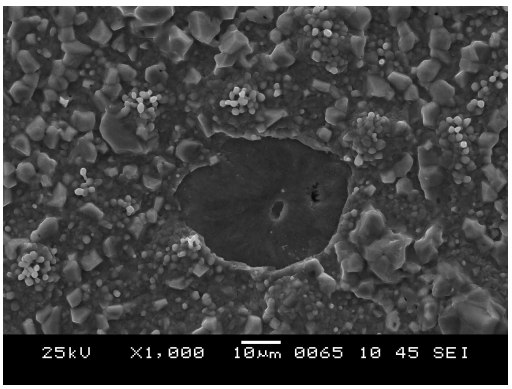

(a)

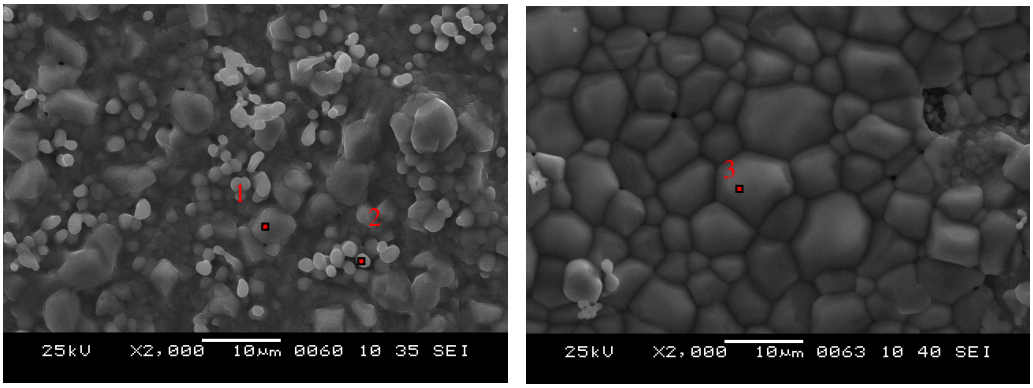

(b) (c)

Figure 6.2 SEM images of polished C-276 sample surface after oxidation at 1150°C/6 h.

Table 6.3 EDS analyses of red areas in Fig.6.2 b and c

Analyses	Concentration, % wt				
	Cr	Ni	Mo	O	Fe
1	4.01	61.72	-	18.12	0.64
2	35.31	15.73	-	26.05	3.05
3	2.95	74.68	-	12.86	2.38

6.3 Results and Discussion for Group 2 Tests

6.3.1 Appearances of Samples after Oxidation Tests

Color changes observed for sample surfaces after oxidation tests in this group are given in Table 6.4.

Table 6.4 Apperances of C-276 and C-22 sample surfaces after oxidation tests of Group 2

	C-276 sample	**C-22 sample**
After 500^{0}C/30 min.	No color change	No color change
After 700^{0}C/30 min.	Light blue	Dark blue
After 800^{0}C/30 min.	Yellow (yellowish brown areas are observed)	Blue (yellow areas are observed)
After 900^{0}C/30 min.	Yellow areas turned green, Brown areas are also observed	Dark grey
After 1150^{0}C/30 min.	Dark grey	Light grey
After 1150^{0}C/ 6 h	Dark grey	Light grey

6.3.2 Mass Changes

Mass changes of the alloy samples after oxidation test are given in Table 6.5 for each cycle. As seen in Table 6.5, there were no considerable changes in sample masses after 1150^{o}C/30 min. Spalled oxide scales were not observed up to the 1150^{0}C/6 h oxidation test for both alloy samples. Significant mass changes were observed for both alloy, only after the 1150^{o}C/6 h test. The approximate amounts of scale collected were 0.0047 g for the C-276 sample and 0.0004 g for the C-22 sample. Mass gain were 0.0003 g/cm^2 for the C-276 sample but only 0.0008 g/cm^2 and for C-22.

Table 6.5 Mass changes of samples after oxidation test in Group 2

Oxidation Tests Conditions	**Mass change of C-276 sample (±0.0001)** (Mass before oxidation=1.5685 g)	**Mass change of C-22 sample (±0.0001)** (Mass before oxidation=1.5025 g)
After 500^{0}C/30 min.	0.0000	0.0001
After 700^{0}C/30 min.	0.0000	0.0001
After 800^{0}C/30 min.	0.0000	0.0001
After 900^{0}C/30 min.	0.0001	0.0001
After 1150^{0}C/30 min.	0.0008	0.0008
After 1150^{0}C/6 h	0.0009*	0.0020*

*Total mass change samples at the end of 1150^{o}C/6 h test (including spalled scales).

6.3.3 SEM Images and EDS Analyses after Oxidation Tests

6.3.3.1 SEM Images and EDS Analyses after 500^{o}C/30 minute

SEM migrographs in Fig. 6.3 a and b show the C-276 and C-22 sample surfaces, at the end of oxidation test at 500^{o}C. In the photographs obtained by BE imaging, the bright regions clearly shows the location of that heavy elements like Mo and W. On these surfaces of alloys, grinding (with sandpaper) marks are still visible. It is clear that, at this temperature, a thick protective oxide scale did not form over the surfaces.

It is understood from EDS analyses that oxygen concentration was low for both sample surfaces (Table 6.6 and 6.7) . EDS data for these bright areas, suggested that they are Ni-Mo-W intermetallic phases. For the C-276 sample, larger such intermetallic phase precipitates were observed. As for the C-22 surface, precipitates were much smaller however with a more uniform distribution over the surface as seen in Fig. 6.3b.

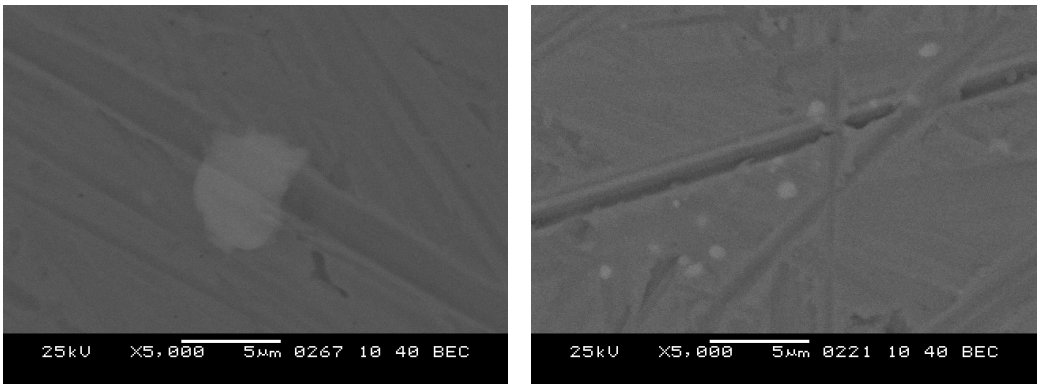

(a) (b)

Figure 6.3 SEM micrographs of surface microstructure of (a) C-276 and (b) C-22 samples after oxidation tests at 500°C/30 min.

Table 6.6 EDS analyses results of bright and dark areas seen in Fig. 6.3 a

In C–276 sample	Concentration, %wt					
	Cr	Mo	Fe	O	W	Ni
Bright area	11.82	40.04	3.15	3.94	15.02	26.01
Dark area	14.69	13.89	5.63	2.91	8.63	54.22

Table 6.7 EDS analyses of bright area seen in Fig. 6.3 b

In C-22 sample	Concentration, %wt					
	Cr	Mo	Fe	W	O	Ni
Bright area	19.07	23.07	4.47	8.98	3.28	41.09

6.3.3.2 SEM Images and EDS Analyses after 700°C/30 minute

Fig. 6.4 a and b show surface morphologies of two different alloy samples oxidized at 700°C/30 min. These SEM photos were taken from surface areas

different than those examined at the end of the 500°C/30 min test. At both alloy sample surfaces, small bright areas were observed in these BE images (Fig. 6.4 a, b). In these location, the oxygen concentration, compared to surfaces oxidized in the 500°C/30 min test, was slightly higher (Table 6.8). Presence of grinding marks at these surfaces indicated that sufficiently thick oxide scales were not formed during this test .

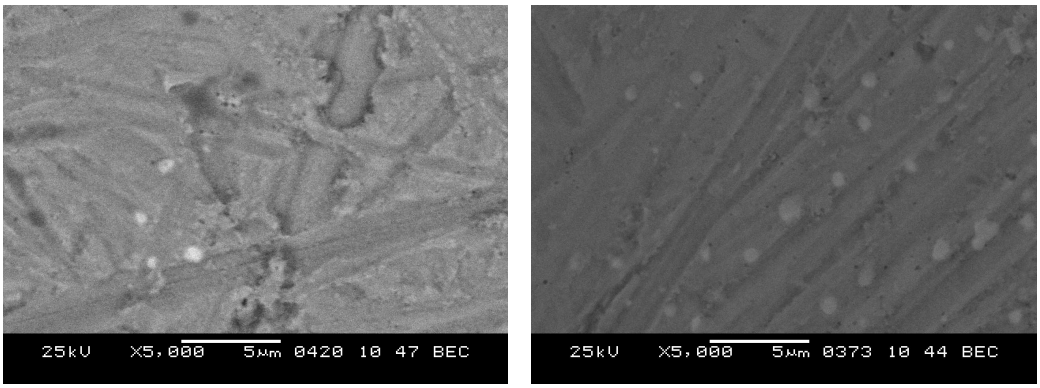

(a) (b)

Figure 6.4 SEM micrographs of surface microstructure of (a) C-276 and (b) C-22 samples after oxidation tests at 700°C/30 min.

Table 6.8 EDS analyses of bright areas seen in Fig. 6.4 a and b

	Concentration, %wt					
	Cr	Mo	Fe	O	W	Ni
Bright area in C-276	13.72	21.93	4.46	6.64	8.16	45.07
Bright area in C-22	19.47	21.45	3.69	9.41	7.19	38.77

6.3.3.3 SEM Images and EDS Analyses after 800°C/30 minute

Fig. 6.5a and b show the surface morphology of C-22 sample oxidized at 800°C/30 min. EDS analyses results from the bright area (in BE mode) show that there is a decrease in Mo concentration. (Bright areas are areas rich in Mo, origininally) However Mo concentration was high in area A at the (SE image) same location. Oxygen concentrations in areas A and B were higher than in C. These results suggested scale formation over these bright areas (Table 6.9).

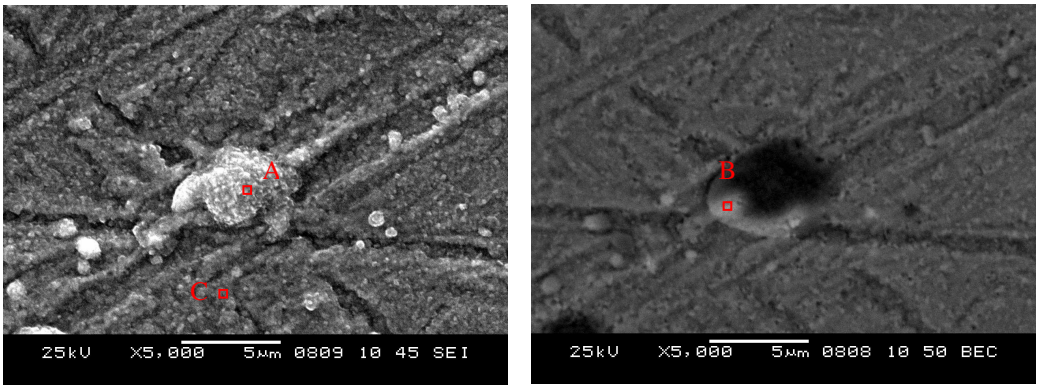

(a) (b)

Figure 6.5 (a) SE and (b) BE images of C-22 sample after oxidation test at 800°C/30 min.

Table 6.9 EDS analyses of red areas selected in Fig. 6.5 a and b

Analyses	Concentration, %wt					
	Cr	Mo	Fe	O	W	Ni
A	24.41	21.54	2.82	12.37	10.23	28.61
B	33.43	8.61	3.00	23.86	5.77	25.30
C	18.52	11.75	4.69	6.49	4.40	54.13

6.3.3.4 SEM Images and EDS Analyses after 900°C/30 minute

After the 900°C/30 min test, no bright area was seen neither on C-276 nor C-22 surfaces. (Fig. 6.6 a and b) This observation was consistent with the previous results. At higher oxidation temperatures, surfaces of samples were oxidized (scale formation) making the detection of the Mo-rich areas difficult. In order to confirm this hypothesis, a new Mo-rich diamond polished C-276 sample was used. Before oxidation, intermetallic precipitate was found at the surface and analysed by EDS. (Fig. 6.7a) Then the sample was oxidized at 900°C for 1 hour. After oxidation the same precipitate was found at the surface and its properties were examined. SE image of intermetallic precipitate is shown in Fig. 6.7b. EDS analyses results showed that a Ni-rich scale was formed over the Ni-Mo intermetallic phase. (Table 6.10) Because of this reason, intermetallic phase did not appear bright in BE image any more (Fig. 6.8).

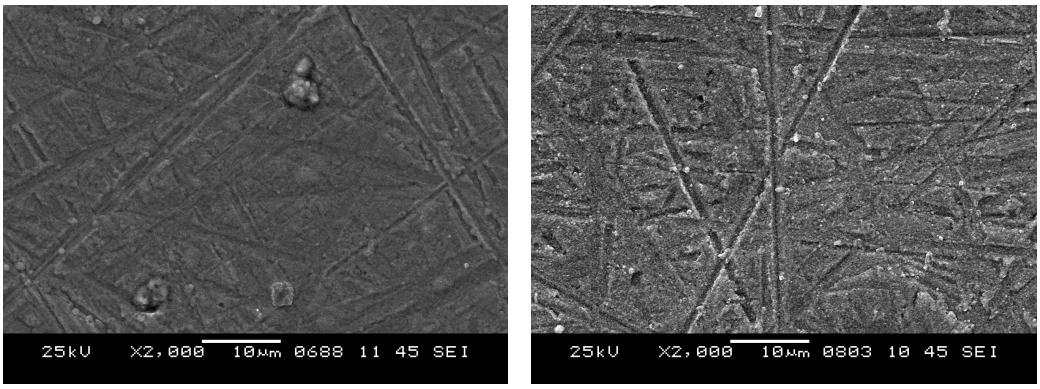

(a) (b)

Figure 6.6 SEM micrographs of surface microstructure of (a) C-276 and (b) C-22 samples after oxidation tests at 900°C/30 min.

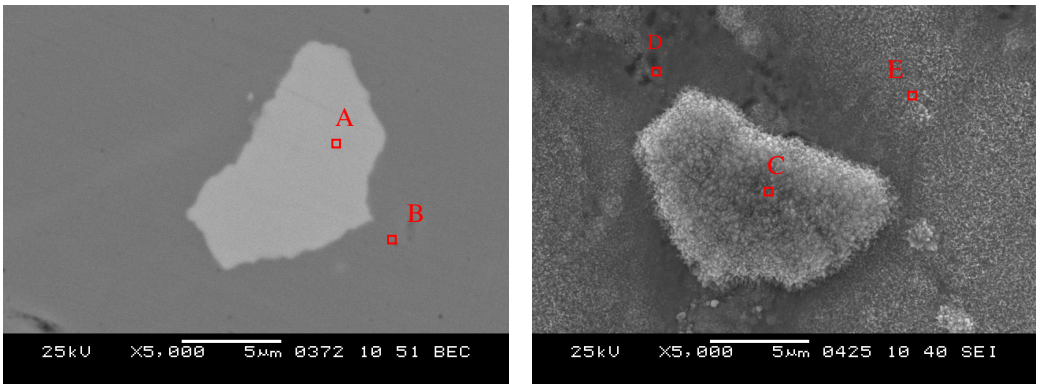

(a) (b)

Figure 6.7 SEM micrographs of polished C-276 surface (a) before and (b) after oxidation tests at 900°C/1 h.

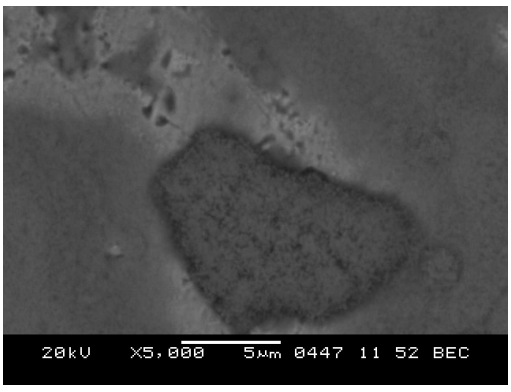

Figure 6.8 SEM micrographs of C-276 after oxidation tests at 900°C/1 h.

Table 6.10 EDS analyses of red areas selected in Fig. 6.7 a and b

Analyses	Concentration, %wt					
	Cr	Mo	Fe	O	W	Ni
A	11.47	40.6	3.26	1.80	14.61	28.23
B	15.20	14.45	5.67	1.20	7.01	56.62
C	6.79	14.25	5.27	25.13	5.69	42.84
D	13.66	12.26	5.40	13.19	5.95	49.52
E	14.24	12.25	4.89	18.32	5.35	44.92

6.3.3.5 SEM Images and EDS Analyses after 1150^{o}C/30 minute

Compared to previous experiments, at this temperature surface morphology changed and scales with ordered geometric crystals were observed over the samples (Fig 6.9 a and b). EDS analyses showed that surfaces of both samples became richer in chromium. SEM images taken at the same magnification showed that, morphologies of the oxide crystals grew on the C-276 surface was different than those formed on the surface of C-22 sample. However compared to the results obtained at lower temperatures, crystalline scale formation on both alloy surfaces was evident after this high temperature test.

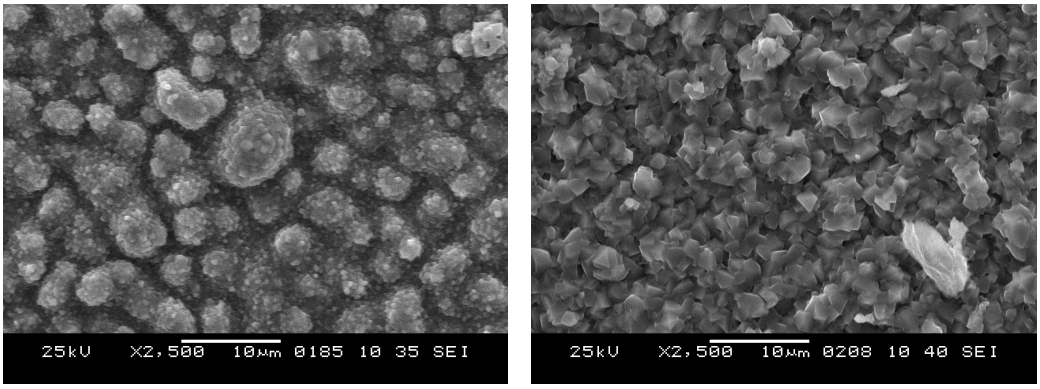

(a) (b)

Figure 6.9 SEM micrographs of general surface microstructure of (a) C-276 and (b) C-22 after oxidation tests at 1150^{o}C/30min.

SE and BE images of cracked oxide scale on C-276 sample surface after 1150^{o}C/30 min is given in Fig. 6.10. EDS analysis results showed that Mo concentration was high in cracked oxide scale. (Table 6.11). In Fig. 6.11, spalled areas on C-22 sample surfaces were shown. Results of EDS analyses from the bright

areas of the C-22 sample showed the same Mo amount that was similar to the test the nominal composition of the alloy (Table 6.12).

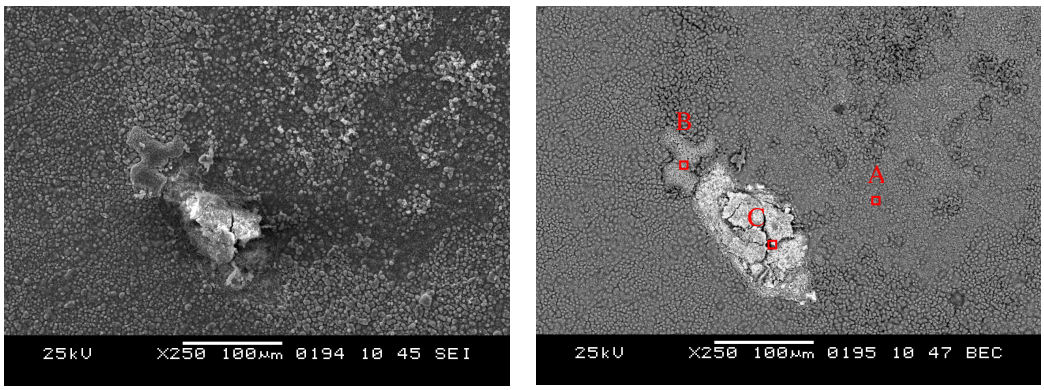

(a) (b)

Figure 6.10 (a) SE and (b) BE images of bright areas in surface microstructure of C-276 after oxidation tests at 1150°C/30min.

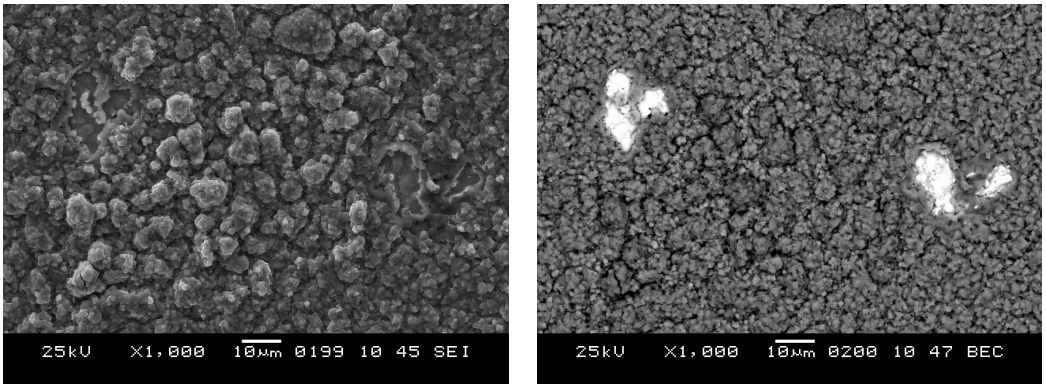

(a) (b)

Figure 6.11 (a) SE and (b) BE images of bright areas surface microstructure of C-22 after oxidation tests at 1150°C/30min.

Table 6.11 EDS analyses of red areas selected in Fig. 6.10 b

Analyses	Concentration, %wt					
	Cr	Mo	Fe	O	W	Ni
A	77.41	0.29	1.64	14.05	-	5.95
B	5.69	0.10	-	9.93	-	80.85
C	20.79	20.95	-	21.43	8.33	28.48

Table 6.12 EDS analyses of bright and dark areas seen in Fig. 6.11 b

Analyses	Concentration, %wt					
	Cr	Mo	Fe	O	W	Ni
Dark area	75.56	0.14	-	23.30	0.98	-
Bright area	14.48	13.06	5.37	2.58	4.82	59.67

An image taken from oxide free (spallation) area is shown in Fig. 6.12 and EDS results of bright area is given in Table 6.13. Mo concentration in this area is lower than its nominal value, too.

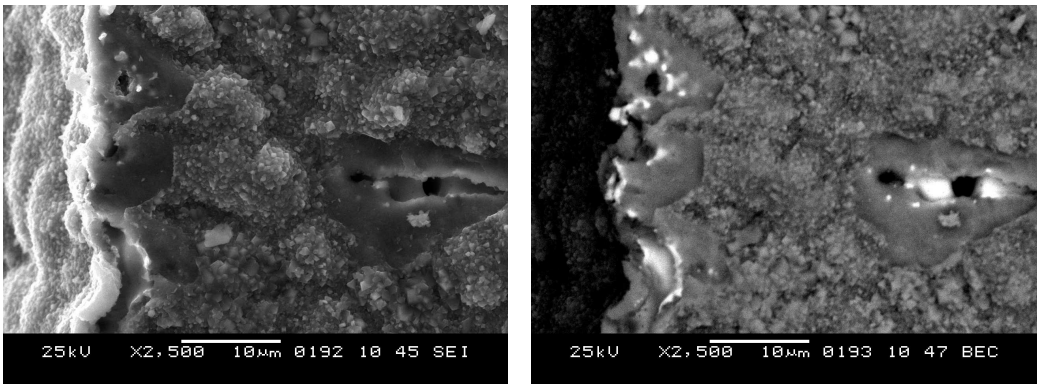

(a) (b)

Figure 6.12 SEM micrographs of C-276 after oxidation tests at 1150 °C/ 30 min (a) in SE and (b) in BE mode.

Table 6.13 EDS analysis of bright areas seen in Fig. 6.12

	Concentration, %wt					
	Cr	Mo	Fe	O	W	Ni
Bright area	11.94	8.97	5.92	3.91	-	69.24

6.3.3.6 SEM Images and EDS Analyses after 1150°C/6 hour

In this test, the samples which had been oxidized for 30 minutes between temperatures 500°C and 1150°C consequtively, were further oxidized at the maximum test temperature (1150°C) for an additional 6 hours. In Fig. 6.13 SEM images of the alloy samples are shown. Scale spallation areas on both sample surfaces are clearly visible in these photos. Similar to scales grown at 1150°C/30 min., morphologies of oxide scales over the samples were different that crystals still covers the surface disorderly. In Fig. 6.14 SEM images of oxide layers are shown. According to the EDS analysis in Table 6.14, area A is Ni-rich layer, on this layer Cr_2O_3 layer (area B) and on the top a layer rich in Ni and Cr element was seen (small grains are rich in Ni, large crystalline structures are rich in Cr).

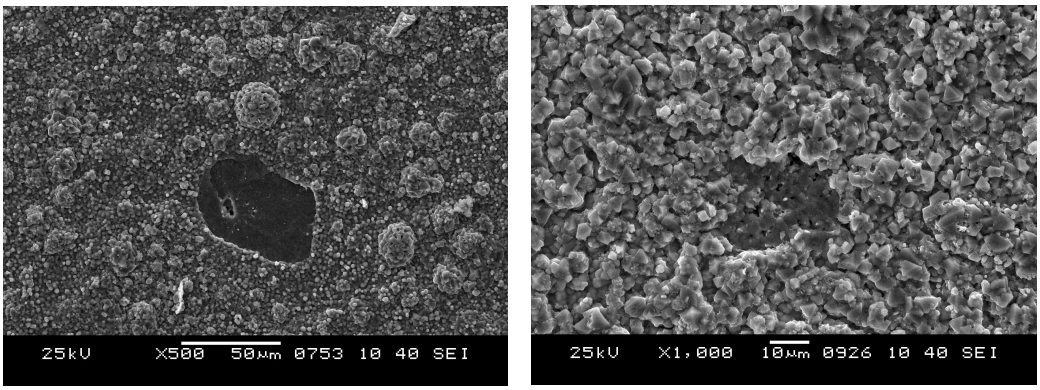

(a) (b)

Figure 6.13 SEM micrographs of surface microstructure of C-276 (a) and C-22 (b) after oxidation tests at 1150°C/6 h.

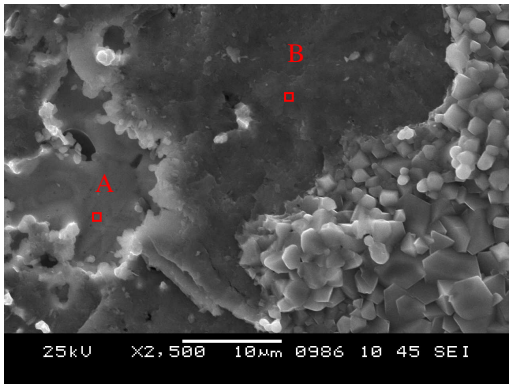

Figure 6.14 High magnification of the spallation area of C-276 after oxidation tests at 1150°C/6 h.

Table 6.14 EDS analyses of red areas selected in Fig. 6.14

Analyses	Concentration, %wt					
	Cr	Mo	Fe	O	W	Ni
A	4.59	12.95	5.85	-	-	75.78
B	84.73	0.14	-	15.11	-	-

6.3.3.7. SEM Images of Spalled Oxide Scale after 1150°C/6 hour

A piece of the scale spalled, from the sample, into the crucible was recovered and examined by SEM/EDS. BE image of this spalled oxide scale is shown in Fig. 6.15 a. Element mapping of the selected area shown in BE mode showed that the bright internal layer of the scale formed was rich in Mo. Over this Mo-rich layer, Cr-rich

and Ni-rich layers were formed on the top of each other (layer by layer). The top large grained layer was rich in Ni.

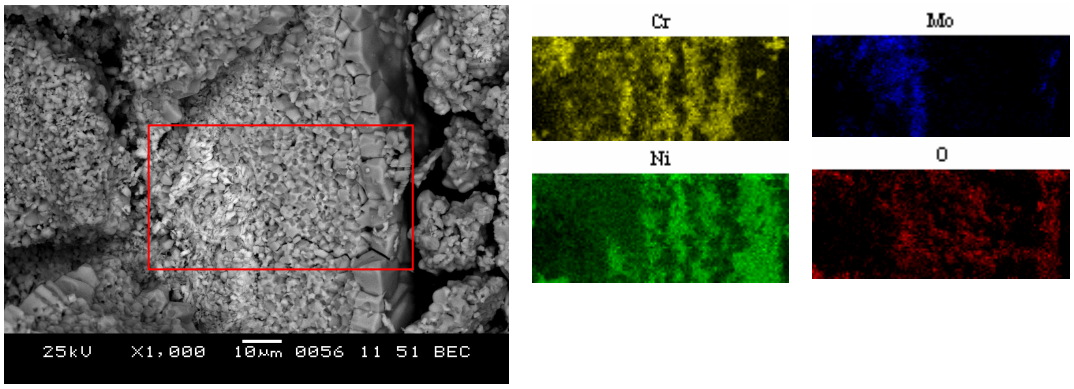

(a) (b)

Figure 6.15 SEM micrographs of spalled oxide scale from C-276 after oxidation tests at 1150 °C/6h (b) element mapping of selected area (a)

6.4 Results and Discussion for Group 3 Tests

6.4.1 Appearances of Test Samples after the Oxidation Test

Fig. 6.16 a and b, show the alloy samples hanging in their respective crucibles at the end of the test. It is obvious that the amount of scale spallation was higher for the C-276 sample. Inside the crucible containing the C-276 sample, areas with yellowish brown color were visible at surfaces facing the sample. However, a similar color change was not observed inside the crucible containing the C-22 sample. No color change is observed also inside surface of crucible used in short time cyclic (Group 2) tests.

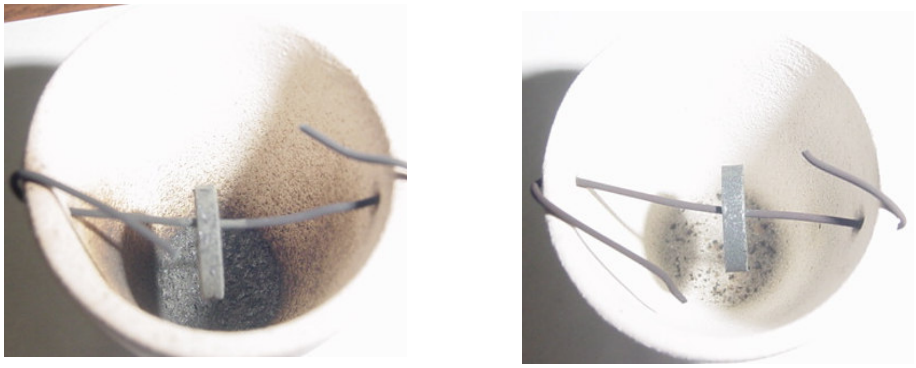

(a) (b)

Figure 6.16. Appearance of (a) C-276 and (b) C-22 samples in crucible after oxidation tests.

6.4.2 Mass Change

Table 6.15 shows mass changes observed for the alloy samples. Negative values indicate that both samples lost mass during the test. For the C-276 sample, the mass loss per unit surface area was higher. Scale spallation from sample surfaces is one of the reasons for the observed negative mass changes. The approximate amounts of scale collected were 0.1200 g for the C-276 sample and 0.0017 g for the C-22 sample.

Table 6.15 Mass changes of alloy samples after oxidation test

Alloys	Mass before oxidation (W1) g	Mass after oxidation (W2) g	Mass change (ΔW=W2-W1) g	Mass change/ surface area g/cm^2
C-276	1.4877	1.4587	-0.0213	-0.8923
C-22	1.5136	1.5116	-0.0020	-0.0842

6.4.3 SEM Images and EDS Analyses

6.4.3.1 SEM Images and EDS Analyses of Samples after Oxidation Tests

SEM micrographs in Fig. 6.17 a and b show the C-22 and C-276 sample surfaces, respectively, at the end of the oxidation test. For the C-22 sample, a uniform distribution of small scale-free (spallation) areas can be seen at the surface (Fig. 6.17a). However, such areas formed on the C-276 surface were much wider.This difference in scale spallation behavior is better observed in the high magnification photographs of Fig. 6.17 c and d. In these photographs obtained by secondary electron (SE) imaging, scale spallation areas appear darker. EDS analyses indicated that darker areas shown in Fig. 6.17c and d were rich in Cr whereas the bright areas contained mainly Ni and Cr. During SEM observation of the product scales it was frequently observed that Mo was present in the areas from which scales spalled off. In Fig. 6.18 a, one such location is shown for the C-22 sample surface. In the photograph of Fig. 6.18 b which was obtained by BE imaging, the bright appearing region clearly shows that heavy elements like Mo and W were present at this

location. In Table 6.16, results of the EDS analyses conducted in the dark and bright areas in Fig. 6.18 b are given.

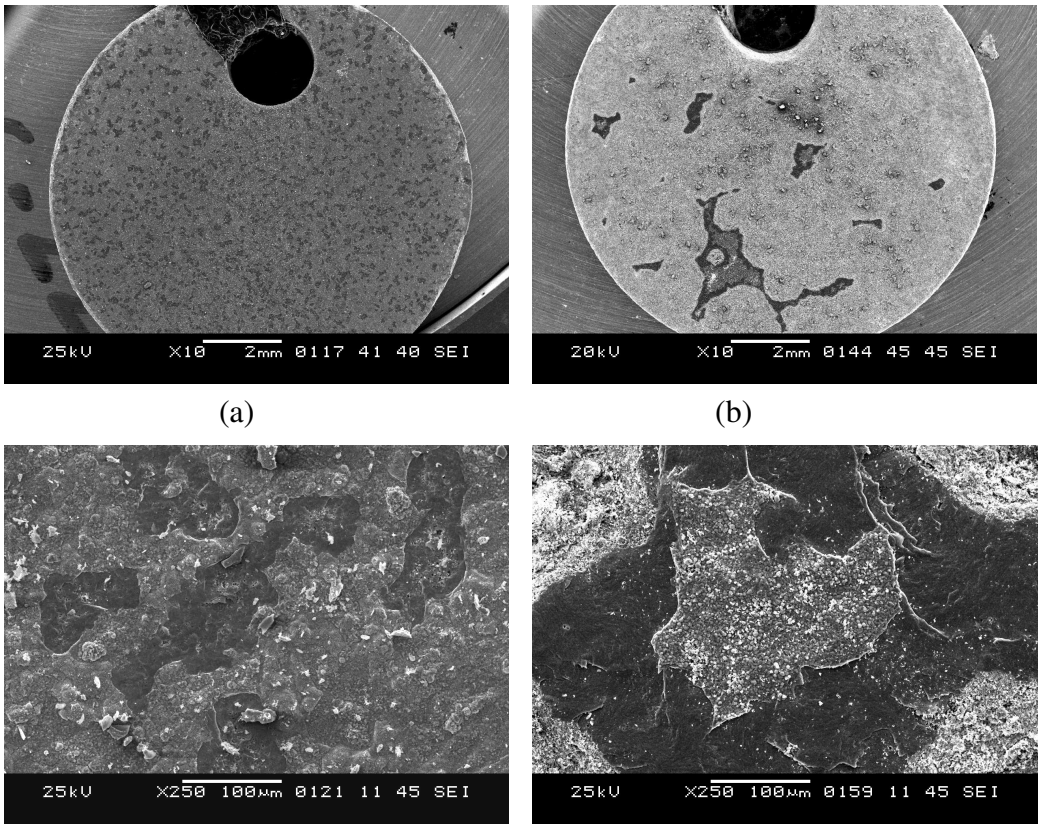

Figure 6.17 SEM micrographs of surface microstructure of C-22 (a, c) and C-276 (b, d) after oxidation tests.

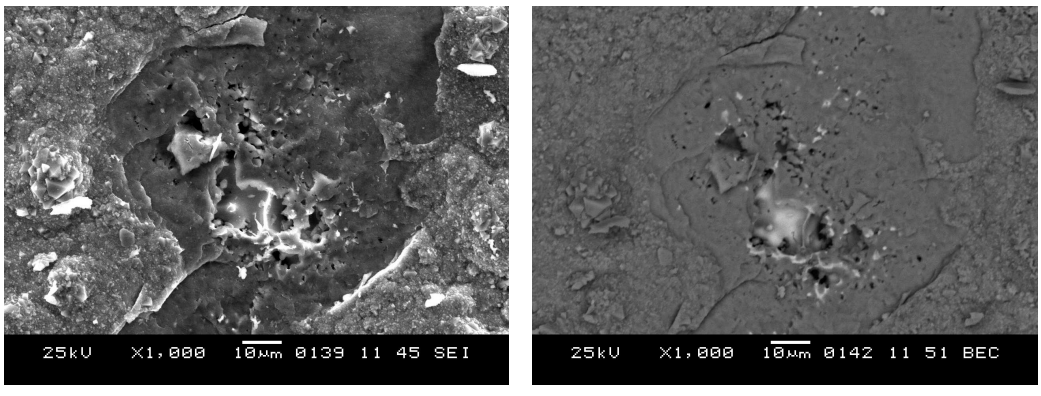

Figure 6.18 (a) SE image (b) BE image of surface microstructure of C-22 after oxidation test.

Table 6.16. EDS analyses of C-22 surface area seen in Fig. 6.18a

	Concentration, %					
	Mo	Cr	W	Ni	O	Fe
Bright area	13.46	13.35	4.29	61.07	2.54	5.27
Dark area	0.11	78.49	0.87	0.71	19.81	-

EDS linescan analyses showed that while Ni, Mo, W amounts were high at the brightest region seen in the SE image of Fig. 6.19, Cr content was lower decline. Oxygen concentration remained unchanged along the scanned distance.

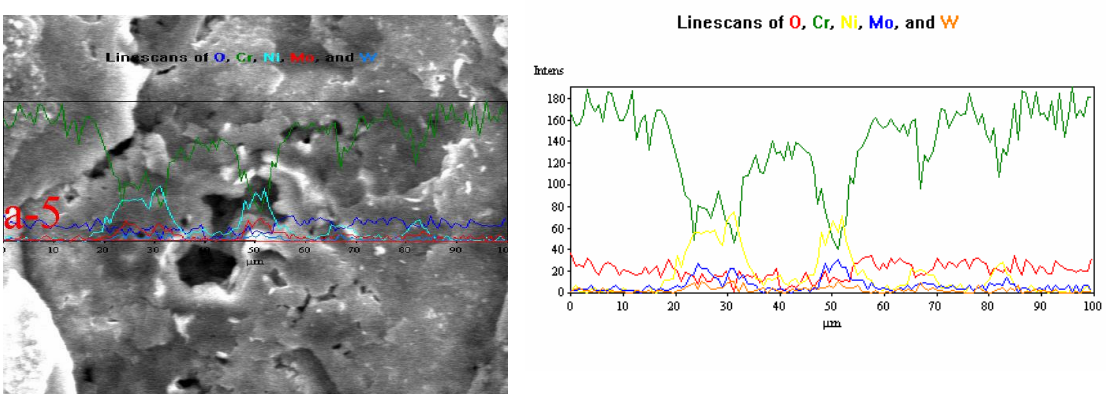

(a) (b)

Figure 6.19 (a) SE image and (b) linescan analysis of C-22 after oxidation test

6.4.3.2 SEM Images and EDS Analyses of Ceramic Crucibles

In Fig. 6.20, BE image and EDS mapping of the internal surface of the crucible used for the C-276 sample are shown. The image location corresponds to the area whereyellowish brown coloring was visually observed after the oxidation test. Although the BE image indicated the presence of heavy elements in this area, it was obvious from the EDS analysis that they contained mainly Mo. This result clearly showed that Mo was transported from the C-276 sample onto the crucible surface during the test. In Fig. 6.21 a and b SEM image of the internal surface of crucible piece is seen at a higher magnification. The SE image in Fig. 6.21b was taken from the area seen in 6.21 a. In this area, crystals and needle-shaped structures are visible on the surface where color changing was observed. According to the EDS analyses, weight percentages, in this areas of Mo, W and O were 41.94, 25.30 and 20.47, respectively. These values show that the crystalline deposits were most likely of Mo-

oxides and W-oxides which formed during the test, evaporated and condensed on the color crucible surfaces.

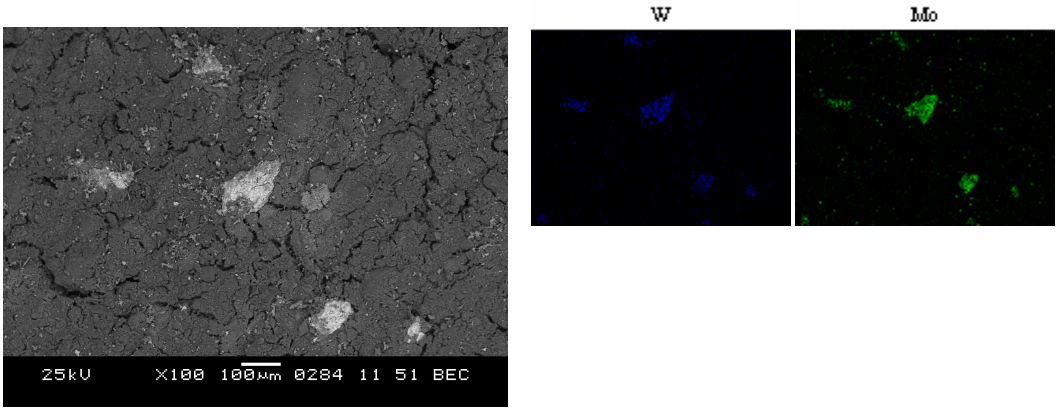

(a) (b)

Figure 6.20 (a) SEM image of the crucible internal surface where color chancing is observed (b) Mo and W elements mapping of the area in (a).

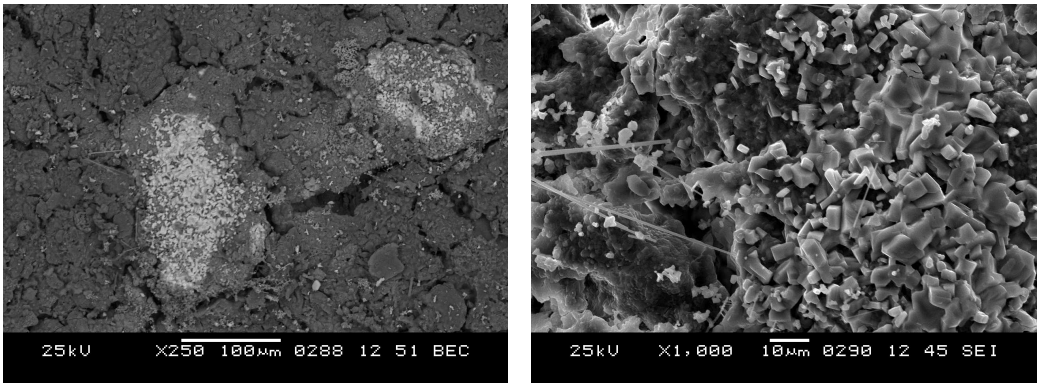

(a) (b)

Figure 6.21. (a) SEM image of the crucible internal surface where color chancing is observed at high magnification in BE mode (b) in SE mode.

6.*4.3.3 SEM Images and EDS Analyses of Spalled Oxide Scales*

In Fig. 6.22, on SE image of oxide scale pieces spalled off from the C-276 sample after this oxidation test are seen. In BE mode a small but bright areas were found EDS analysis of this area, detected %23.31 Mo.

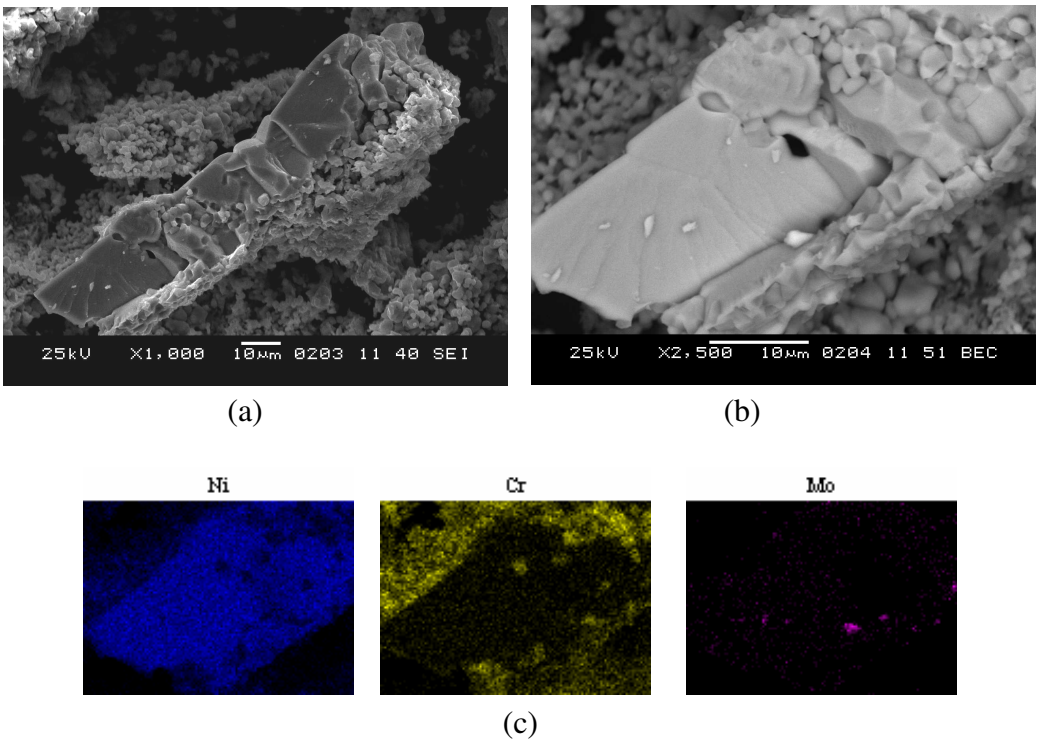

Figure 6.22 (a) SE image (b) BE image of oxide scales spalled from C-276 after oxidation test , (c) Ni, Cr and Mo elements mapping of the area in (a).

6.4.3.5 SEM Observation of Sample Cross-sections

Besides in-plan observation of the product scales, in Fig. 6.23, BE image of C-276 sample cross section is shown. A continous and non-porous Cr-rich layer formation was evident on the sample surface. Over this, a layer containing oxides of Cr and Ni was present. This could be of a spinel phase. The top layer in the Picture is Mo and Ni-rich. These EDS analyses results indicated the presence of Cr_2O_3 at the scale/alloy interface (Table 6.17).

SEM images taken from C-22 and C-276 sample cross sections at same magnification (Fig. 6.24 a and b) showed a non uniform internal oxidation zone for the C-22 sample whereas this zone was more uniform for the C-276 alloy.

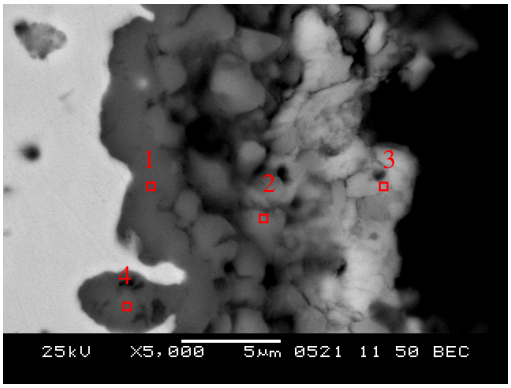

Fig. 6.23 Cross-section of C-276 sample.

Table 6.17 EDS analyses of red areas selected in Fig. 6.23

Analysis no	Concentration, %wt				
	Cr	Ni	Mo	O	Fe
1	63.73	4.59	0.97	28.29	1.13
2	36.28	22.11	2.52	32.70	3.56
3	13.07	22.55	26.37	24.71	1.75
4	55.60	11.66	2.71	25.81	1.45

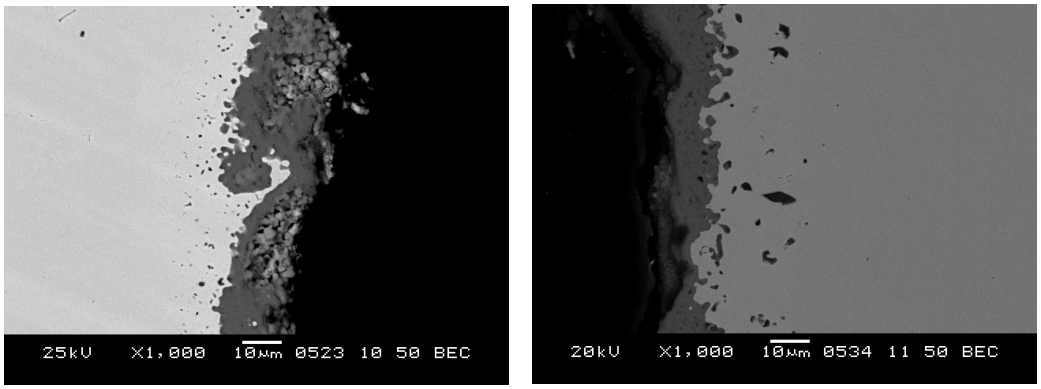

(a) (b)

Figure 6.24. BE image of cross-section of (a) C-276 and (b) C-22 samples.

6.4.3 XRD Analyses of Selected Scales

After the 42 hour oxidation test at 1150°C, the outer surface of the C-276 and C-22 samples were investigated by x-ray diffraction (XRD). Scales spalled from C-276 sample surface was also investigated. The result of these analyses are shown in Fig. 6.25–6.27. It is noted that the scale formed at the surface of C-276 alloy contained crystalline oxide phases like NiO, Cr_2O_3 and spinels ($NiCr_2O_4$ and $NiMoO_4$), however at the surface of C-22 sample $NiCr_2O_4$ spinel and Cr_2O_3 are detected. NiO and spinels ($NiCr_2O_4$ and $NiFe_2O_4$) were detected from the analysis of spalled oxide scale pieces.

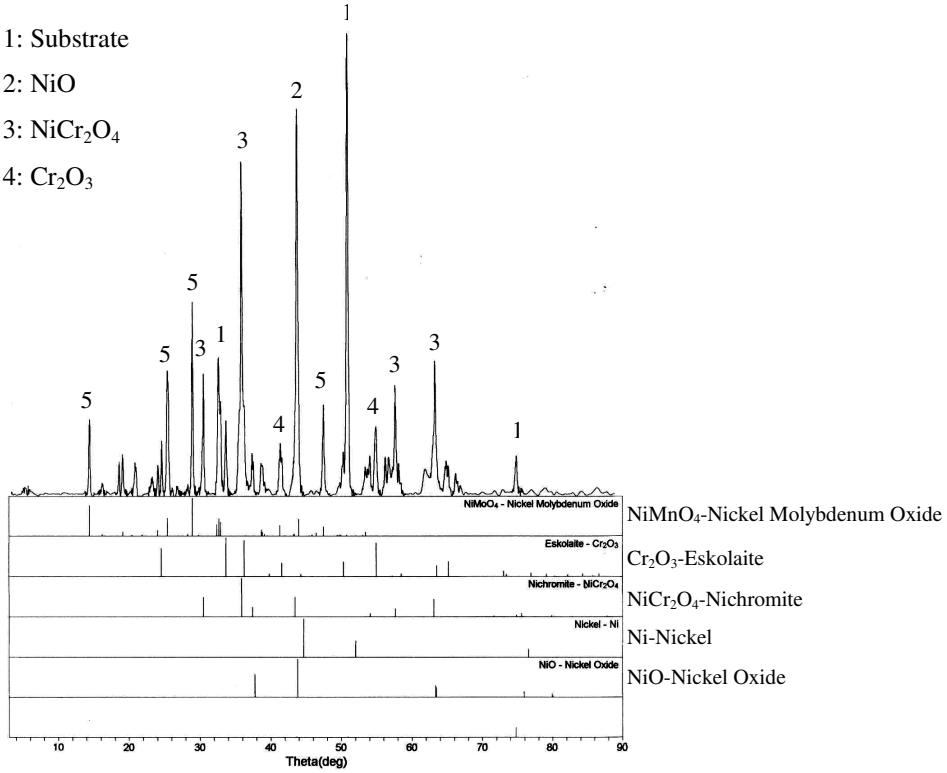

Figure 6.25 XRD analysis of the C-276 surface after oxidation.

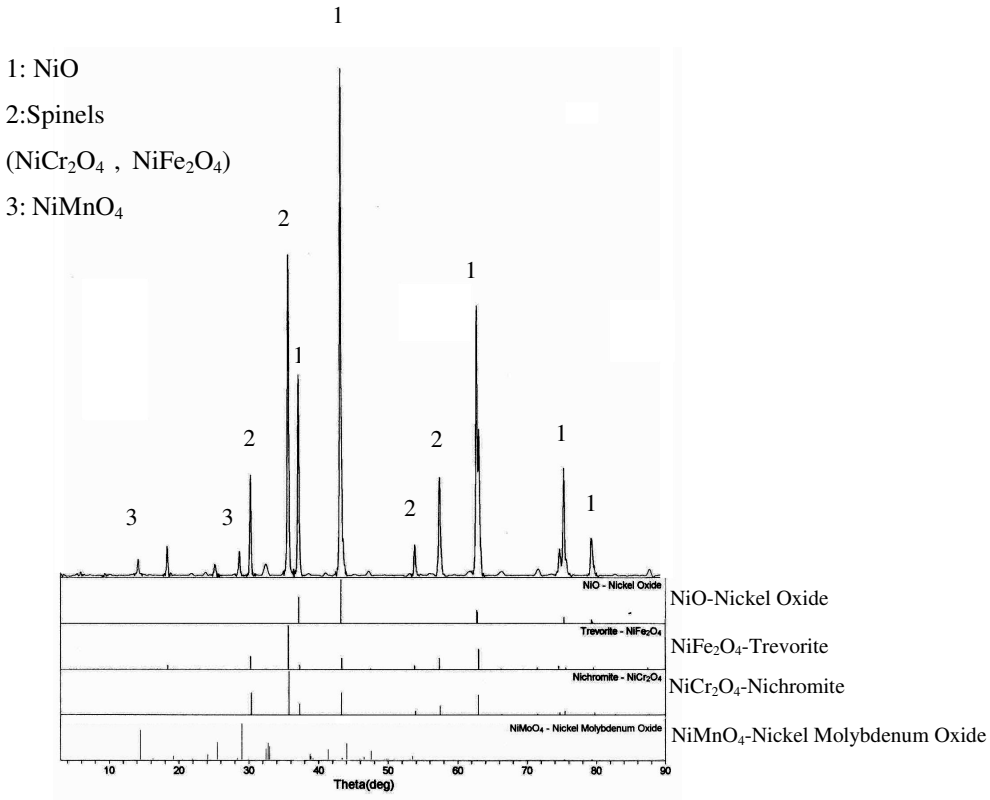

Figure 6.26 XRD analysis of the spalled oxide scales from C-276 surface.

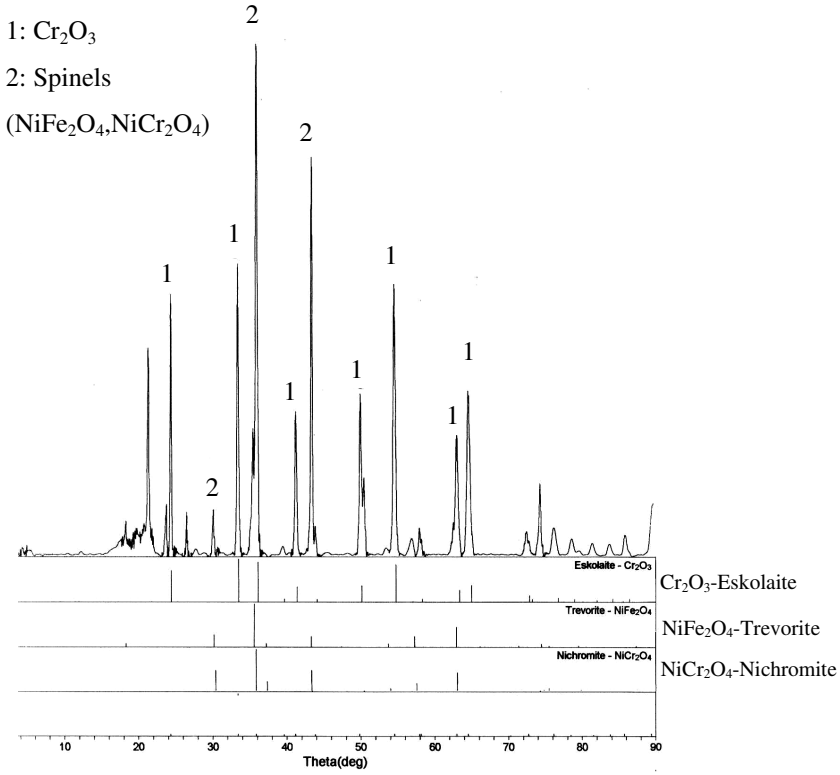

Figure 6.27 XRD analysis of the C-22 surface after oxidation.

Alloys C–22 and C–276 studied in this work are not high temperature alloys. However, they were chosen for this work because they contain more than 10% Mo in their composition. Since investigation of the effect of Mo on corrosion is one of the aims of this study and they were already available, it was decided to use these alloys.

Results of Group 1 tests indicated that, mass gain of the alumina polished C–276 sample was higher than the mechanically (800 grit sandpaper) ground C–276 sample (Table 6.2). It is reported, in other studies, that smooth surfaces such as a polished surface, oxidize more slowly than rough surfaces obtained by machining, abrading or etching (Milley, n.d.). Specimens abraded mechanically could develop more stoichiometric Cr_2O_3 oxide layers at a faster rate during early stages of oxidation causing effective diffusion barrier formation and hence reduction in the oxidation rate of the sample (Kuiry, Seal, Bose, Roy, 1994). The influence of roughness however was observed to be greatest at the beginning, and diminishes as the original surfaces corrodes away (Austin & Gurry, n.d.). In the Group 1 tests conducted for 6

hours, it was found that the polished C–276 alloy sample with a lower surface roughness exhibited a higher oxidation rate.

Results of the oxidation tests conducted showed that high temperature oxidation in air caused formation of Ni- and Cr-rich oxide scales over both alloys. This was expected since the alloys are Ni-base and have Cr contents more than 15%. However, SEM observations suggested that the amount of Ni-rich oxides was higher in the scales grown over the C–276 alloy samples. This is reasonable since this alloy had a lower Cr content (15%) than the C–22 alloy (22%).

It is expected that significant thermal stresses arose as a result of heating and cooling (thermal cycling) of samples, especially during the tests longer than 6 hours. Excluding the low temperature tests, after all the tests conducted at high temperatures ($T>1000^oC$), cracking and spalling of scales were observed. Spallation of scales was found to be larger for the C–276 alloy samples. Lower Cr content of the C–276 alloy is thought to be one of the reasons for this result. During oxidation, both NiO and Cr_2O_3 oxide grains form on alloy surfaces. Because NiO has a higher growth rate, NiO crystals form a layer which overgrows the Cr_2O_3 crystals formed at the alloy/scale interface. Because C–276 has a lower Cr content, chromia layer formed on this alloy might not have protected further growth of the NiO scale. During thermal cycling, this thick and porous NiO rich scale spalled easily because of thermal stresses developed. However, the Cr_2O_3 scale formed on the C–22 sample was believed to be protective against thick NiO layer formation. Thus, amount of scale spallation from the C–22 alloy samples was lower.

Test results suggested that Mo content of these alloys was also responsible for the observed poor adherence of oxide scales. As the SEM photos in Fig. 6.18 showed, Mo-rich areas were always present at the locations were scale spallation took place. The MoO_3 phase has a melting temperature of 795^oC and a boiling point of 1150^oC. Since the oxygen partial pressure in air was enough to form the MoO_3 phase during oxidation, formation of MoO_3 gas inside the scale and consequent evaporation would have caused mechanical failure (spallation) of the oxide scale. In this study, more

scale spallation was observed for the C–276 alloy which has a higher Mo content. The effect of gaseous Mo-oxides in alloy oxidation was also discussed in several other studies. (DiStefano & et. al. 2000; Helmik, 2003; Pérez & et. al. 1998)

Experimental evidence for the formation of gaseous Mo-oxides and their escape from the samples during oxidation was obtained in this study as seen in Fig. 6.20 and 6.21. These BE images were taken from the inner surfaces of the ceramic crucible which contained the C–276 alloy whose Mo concentration is high. Crucible walls facing the sample had yellowish brown colored areas which were found to contain large amounts of Mo. Presence of crystals with various morphologies suggested that they were deposited from the vapor phase as in a CVD process.

Besides scale spallation, the loss of Mo (also some W) from the sample during oxidation also complicates the quantative mass change data obtained for the alloy samples. The negative mass change values reported in Table 6.15 for the Group 3 test samples must have been affected by such a vaporization process. Similar results were also reported elsewhere. (DiStefano, Pint, DeVan, 2000)

High temperature oxidation behavior of the test alloys used in this study might have been affected also by the intermetallic compounds (in the form of Ni_xMo_y and Ni_xW_y) which were present in the as-received alloy. In the Mo-rich C–276 alloy, larger particles of such second-phase precipitates were present. In the C–22 alloy, however, such precipitates were much smaller and more uniformly distributed in the alloy as seen in Fig. 6.3. In Fig. 6.17, scale formed on the C–22 sample is shown. The presence of small and uniformly distributed scale-free (spallation) areas suggested that spallation of the scale might have been promoted by the intermetallic phases in the underlying alloy surface. Results obtained for the C–276 alloy also suggested the same possibility.

To explain some other experimental results, behavior of the alloying elements (Cr, Mo) as well as the base metal Ni during oxidation needs to be discussed. Fig. 6.15, for example, shows the microstructure of the scale spalled from the C–276

sample oxidized for 6 hours following several short cycles of oxidation at lower temperatures. EDS analyses results showed that both Cr- and Ni-rich oxides were present in the scale as alternating layers. There is also a Mo-rich layer at the bottom of the scale. It is thought that this scale microstructure is a result of the relative thermodynamic stabilities of oxides as well as the cyclic spallation of the surface scale.

Thermodynamic stabilities of phases depend on their Gibbs free energy of formation. By making using of such data, relative stabilities of compounds can be shown by the so-called Ellingham diagrams. In Fig. 6.28 such a diagram is given. This diagram was plotted for the oxide phases important for this study. For plotting Fig. 6.28, thermodynamic data in Table 6.18 were used. Since Gibbs free energy of formation is a measure of the chemical affinity of the metal for oxygen, larger negative values indicate higher thermodynamic stability for the compound. As seen in the diagram, free energy of Cr_2O_3 formation is the most negative at all temperature. Consequently, Cr_2O_3 is the oxide formed close to the alloy/scale interface where the oxygen partial pressure is the lowest (Table 6.19). At the opposite end of the scale (scale/gas interface) NiO is expected to form because it requires more oxygen to form. Between the Cr_2O_3 and NiO layers, the intermediately stable oxides of Mo and W, should form. However, because of cycling and scale spallation, the sequence of oxide phases in the scale may be changed.

Table 6.18 The standart free energy changes for several reaction

Reaction Code	Reaction	ΔG^o, KJ	Range, K
A	$4/3Cr+O_2=2/3Cr_2O_3$	$\Delta G^o(T)$= -746844+173.2176T	298 - 2100
B	$Mo+O_2=MoO_2$	$\Delta G^o(T)$= -586178.4+-19.2464TlogT+233.4672T	298 - 1300
C	$W+O_2=WO_2$	$\Delta G^o(T)$= -550614.4+153.1344T	298 - 1500
D	$2Ni+O_2=2NiO$	$\Delta G^o(T)$= -524255.2+217.40064T	1725 - 2200
E	$2MoO_2+O_2=2MoO_3$	$\Delta G^o(T)$= -323841.6+163.176T	298 - 1300

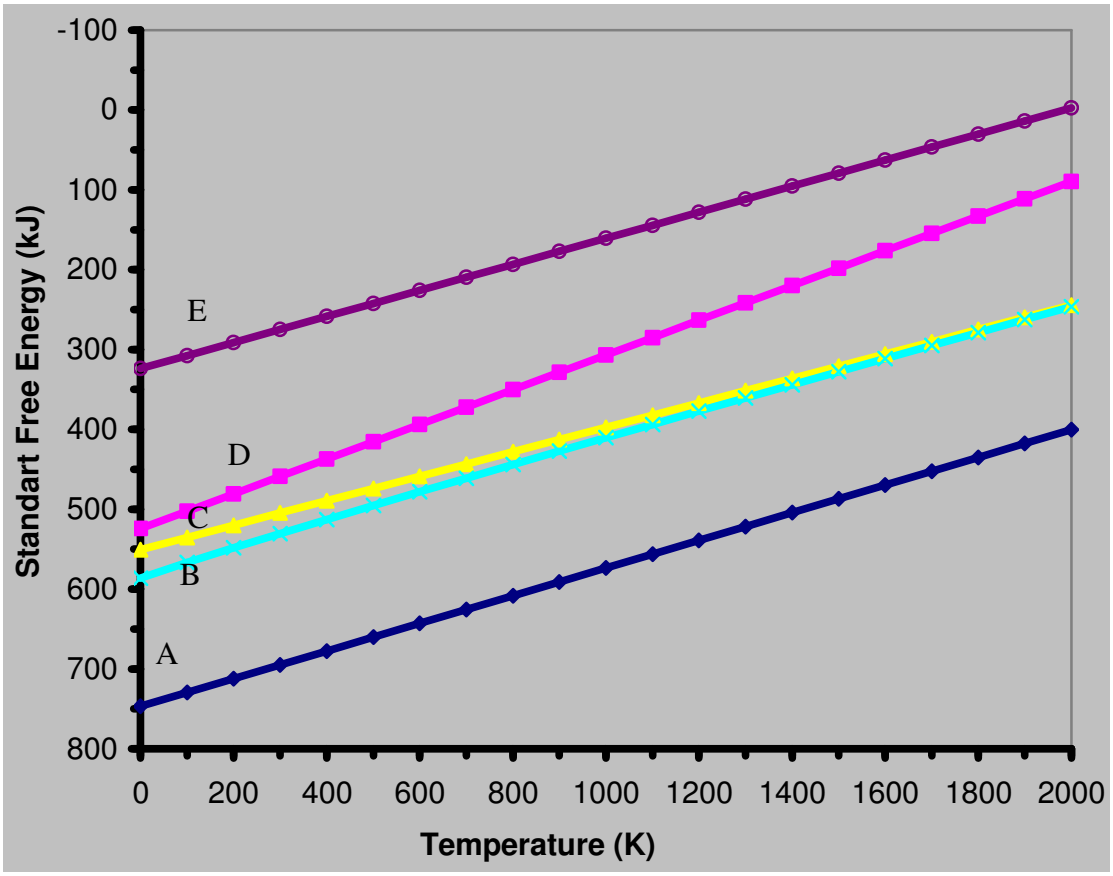

Figure 6.28 Ellingham diagram for selected element

Table 6.19 Partial pressure calculated for formation of oxidation reaction

T, K	Treshold partial pressure for formation of oxidation reaction (P_{O2})				
	$4/3Cr+O_2=2/3Cr_2O_3$	$Mo+O_2=MoO_2$	$W+O_2=WO_2$	$2Ni+O_2=2NiO$	$2MoO_2+O_2=2MoO_3$
773	$3.63x10^{-42}$atm	$4.63x10^{-31}$atm	$5.98x10^{-30}$atm	$8.27x10^{-25}$atm	$4.30x10^{-14}$atm
973	$8.67x10^{-32}$atm	$5.14x10^{-23}$atm	$2.68x10^{-22}$atm	$1.60x10^{-17}$atm	$1.36x10^{-09}$atm
1073	$4.75x10^{-28}$atm	$4.00x10^{-20}$atm	$1.53x10^{-19}$atm	$6.72x10^{-15}$atm	$5.69x10^{-08}$atm
1173	$6.00x10^{-25}$atm	$9.95x10^{-18}$atm	$2.96x10^{-17}$atm	$1.01x10^{-12}$atm	$1.26x10^{-06}$atm
1423	$4.20x10^{-19}$atm	$3.17x10^{-13}$atm	$6.04x10^{-13}$atm	$1.28x10^{-08}$atm	$4.31x10^{-04}$atm

XRD analyses conducted on some of the selected samples and spalled oxide scale pieces showed that in addition to the Cr_2O_3 and NiO phases, Mo and Cr containing spinels were also present in the scales. (Fig. 6.25, 6.26). This result is consistent with the above explanation of scale structure. After the formation of Cr_2O_3, Mo-oxides and NiO in the scale, reactions among these oxide phases would have caused the formation of spinel phase with formulas $NiCr_2O_4$ or $NiMoO_4$.

CHAPTER SEVEN
CONCLUSIONS

Important conclusions of this study are as follows;

- Significant oxide scale formation on Mo-containing C-22 and C-276 Ni-base alloys were observed only at temperatures above 1000^{o}C.

- Although multi-structure scales containing Ni and Cr-rich oxides developed over both alloys, those formed on C-276 were less adherent to their substrates. Mo was present in scales, but its distribution was not uniform.

- BE imaging by SEM indicated that Mo was present in large amounts at areas where scale spallation (detachment) took place over the C–276 alloy which has a lower Cr but a higher Mo content.

- BE imaging and EDS analyses also showed that Mo was present over the inside surfaces of the crucible containing the C–276 alloy sample. This was taken as a proof of Mo loss (volatilization) from this alloy.

- Volatilization of Mo (possibly as MoO_3) is concluded to be an important cause for the observed scale spallation from the test alloys.

- Intermetallic compounds (possibly as Ni_xMo_y and Ni_xW_y) present in as-received alloys. In the Mo-rich C–276 alloy, larger particles of these second-phase precipitates were present. These precipitates might have affected high temperature oxidation behavior of these Mo-containing test alloys.

- Backscattered electron (BE) imaging was found to be an effective technique in this study of alloys containing heavy refractory elements like Mo and W.

- In any oxidation-resistant Mo-rich alloy development work, all these observed effects of Mo on alloy oxidiation should be taken into account.

REFERENCES

Akhtar, A., Hegde, S., & Reed, R.C. (2006). The oxidation of single-crystal nickel-based superalloys. *JOM,* v. 58(1), 37–42.

Alloy Wire International, *Hastelloy C-276 and Hastelloy C-22* (n.d.). Retrieved January 29, 2006, from http://www.alloywire.com.

Austin, J.B., & Gurry, R.W. (n.d.). Iron and steel. *The High Temperature Corrosion* (630-632).

Buckman, R.W. Jr. (1988). Alloying of refractory metals. Walter J.R., Jackson M.R., Sims C. T. (ed.). *Alloying*.(419–421*)*. Metals Park, OH: ASM International.

Betteridge, W., & Shaw, S.W.K. (1987). Development of superalloys. *Materials Science and Technology*, v.3, 682–683.

Davis, J.R. (ed.) (1997). *ASM Speciality Handbook, Heat Resistant Materials* (361–365). Metals Park, OH: ASM International.

DiStefano, J.R., Pint, B.A., & DeVan J.H. (2000). Oxidation of refractory metals in air and low pressure oxygen gas. *International Journal of Refractory Metals & Hard Material,* v.18, 237–243.

Exner H.E. (1985). Scanning Electron Microscope. Mills, K. (ed.). *ASM Handbook, Metallography and Microstructures, Volume 9* (89-103) , Materials Park, OH: ASM International.

Gritsch, M., Piplits, K. H., Hutter, P., Wilhartitz, H., Wildner., H.P., & Martinz (2000). Investigations on the oxidation behavior of technical molybdenum foils by means of secondary-ion mass spectrometry. *Surface Science*, v. 454–456, 284–288.

Habazaki, H., Hon-yashiki, K., Ito, K., Mitsui, H., Kawasashima, A., Asami, K., Hashimoto, K., & Mrowec, S. (1999) Sulfidation and oxidation-resistant alloys prepared by sputter deposition. *Materials Science and Engineering*, A267, 267-276.

Hebsur, M.G., Stephens J.R., Smialek, J.L., Barrett, C.A., & Fox, D.S. (1989). Influence of Alloying Elements on the Oxidation Behavior of $NbAl_3$. Grobstein T.& Doychak (ed.) (171-183). *Oxidation of High-Temperature Intermetallics,*TMS

Helmick, D.A. (2003). High temperature oxidation behaviour of Mo-Si-B base alloys (6-20). University of Pittsburg.

Japan Electron Optics Laboratory (JEOL). A guide to scanning microscope observation (n.d), July, 2006, www.jeol.com.

Johnson, W. A. (1990). Molybdenum, Properties and selection: nonferrous alloys and special purpose-material. Davis, J.R. (ed.) *ASM Handbook, Properties and Selection: Nonferrous Alloys and Special Purpose-Materials, Volume 2* (574–577), Materials Park, OH: ASM International.

Kawagishi, K., Harada, H., Sato, A, & Kobayashi, T. (2006). The Oxidation Properties of Fourth Generation Single-Crystal Nickel-Based Superalloys. *JOM,* 58(1), 43-46.

Kuiry, S.C., Seal, S., Bose, S.K., & Roy, S.K. (1994). Effect of surface preparation on the high-temperature oxidation behavior of AISI 316 stainless steel. *ISIJ International*, v.34, 599-606

Lai, G.Y. (1990a). Section 1:Introduction. *High Temperature Corrosion of Engineering Alloys* (1–4). Metals Park, OH: ASM International.

Lai, G.Y. (1990b). Section 3:Oxidation. *High Temperature Corrosion of Engineering Alloys* (15–46). Metals Park, OH: ASM International.

Lambert, J. B., & Rausch, J.J. (1990). Refractory Metals and Alloys. Davis J.R. (ed.). *ASM Handbook, Properties and Selection: Nonferrous Alloys and Special Purpose-Materials, Volume 2* (557-565), Materials Park, OH: ASM International.

Mankins, W.L., & Lamb, S. (1990). Properties and selection: nonferrous alloys and special purpose-material. *ASM Handbook, Properties and Selection: Nonferrous Alloys and Special Purpose-Materials, Volume 2* (428-445), Materials Park, OH: ASM International.

Mevrel, R. (1987). Cyclic oxidation of high temperature alloys. *Materials Science and Technology*, v.3, 531–535.

Miley, H. A. (n.d.). Fundamental of oxidation and tarnish. *Corrosion Theory* (11-21).

Mizutani, M. (1990). Study on high temperature oxidation of Ni-Cr ceramic alloys. Effects of Cr and Mo*, Aichi Gakain Daiguku Shigakka Ski*, 59-78. Retrieved 2006, from PubMed Articles database.

Pérez, F.J., Otero, E., Hierro, M.P., Gomez, C., Pedraza, F., Segovia J.L., Roman, E. (1998). High temperature corrosion protection of austenitic AISI 304 stainless steel by Si, Mo and Ce ion implantation. *Surface and Coating Technology,* v.108-109, 127-131.

Sridhar, N. (1987). Behavior of nickel-base alloys in corrosive environment. Korb, L.J. (ed). *ASM Handbook, Volume 13. Corrosion* (643-647), Metals Park, OH: ASM International.

Sharma, I.G., Chakroborty, S.P., & Suri, A.K. (2005). Preparation of TZM alloy by aluminothermic smelting and its characterization. *Journal of Alloys and Compounds*, v.393, 122–128.

Smolik, G.R., Petti , D.A., & Schuetz, S.T. (2000). Oxidation and volatilization of TZM alloy in air. *Journal of Nuclear Materials,* v. 283–287, 1458–1462.

Stoloff, N.S. (1990). Wrought and P/M superalloys. Lampman H.F. (ed.). *ASM Handbook Properties and Selection: Irons, Steels and High-Performance Alloys, Volume 1* (950–953). Materials Park, OH: ASM International.

Stott, F.H. (1989). Influence of alloy additions on oxidation. *Materials Science and Technology*, v. 5, 734–740.

Tawancy, H.W., Klarstrom, D. L. & Rothman, M. F. (1984). Development of a new nickel-base superalloy. *Journal of Metal*, v.36, 58–59.

Verhoeven, J.D. (1986). Scanning electron microscope. When, R.E. (ed.). *ASM Handbook, Materials Characterization, Volume 10 (491–515)* , Materials Park, OH: ASM International.

Wallwork, G.R. (1975). The oxidation of alloys. Ziman, J.M. (ed.) *Reports on Progress in Physics v.39* (471-475). Institute of Physics, London.

Wright, I.G. (1987). High Temperature Corrosion. Korb, L.J. (ed). *ASM Handbook, Volume 13. Corrosion* (97–103). Metals Park, OH:ASM International.

Wood, G.C., & Stott, F.H. (1987). Oxidation of alloys. *Materials Science and Technology*, v. 3, 519–523.